Cellular Cooperativity

Modeling collective dynamics of the lizard's inner ear

Olha Fedoryk

Thesis submitted to the Faculty of Graduate Studies in Partial Fulfillment of the Requirements for the Degree of Master of Science

Graduate Program in Physics and Astronomy
York University
Toronto, Ontario
September 2023

Cellular Cooperativity

Modeling collective dynamics of the lizard's inner ear

Olha Fedoryk

Abstract

The ear is sound detector that is remarkably sensitive and selective. As a nonlinear and active system, ears also emit sound, known as otoacoustic emission (OAEs). We investigated the theoretical origins of spontaneous emissions (SOAEs), which appear as idiosyncratic peaks unique to a given ear. Using an established model of locally coupled limit cycle oscillators, we adapted and extended the framework for describing an Anolis lizard ear and explored several specific hypotheses.

We observed that depending on the set of parameters and number of oscillators, the system could become sensitive to initial conditions and stay either stable or unstable. We also conclude that embedding only morphological differences (via frequency or hair cell bundle height) is not enough to generate "unique ears". Finally, we achieved a peak broadening by presenting additive noise to the system both as external and local thermal noise.

To my mother and father,
you taught me the value of curiosity and enjoying the pursuit of knowledge.
Thank you for your support and for making my life full of amazing opportunities.

And to all the brave people of Ukraine...

Acknowledgements

I am grateful for the amazing experience that grad school provided me. I want to acknowledge everyone I crossed path with during these years at York University, without you this time would have not been as complete, memorable and enjoyable as it has been.

First, I want to thank my supervisor, Christopher Bergevin, for being my mentor during these years. Although he always emphasizes that our success depends on us, I am sure that without his support and guidance, I wouldn't be able to succeed. As my supervisor, he taught me how research requires us to be curious, critical, enthusiastic and independent, yet at the same time have people with whom to have a discussion. Those people are our SBL team and I want to thank Rebecca Whiley, Zena Khadour, Filipe Ledo, Junting Jiang, Nikita McKnight, Václav Vencovský, Elizabeth Allison and others. I am grateful for our discussions during journals club, along with your input and support for my research. Even if we didn't have a physical lab you made me feel that lab experience that I was looking forward to gaining during grad school. Also thank you to everyone from the MoH community for inspiring our lab discussions, via your papers or direct communications.

At the same time, I want to thank Mitacs and all the people who made it possible for me to come here to Canada, and have this opportunity to become a Master of Science. I also want to thank all my teachers from Ukraine, who showed me the potential of physics and gave me that boost to move forward.

A special thanks goes to members of my thesis committee, Christopher Bergevin, Joel Zylberberg and Michael Haslam for their valuable input.

Table of Contents

List of Figures

Chapter 1

Introduction

1.1 Background

The ear is an extraordinary signal detector, it exhibits numerous impressive characteristics despite such limitations as thermal noise, operating range of neural responses, and fluid mechanics (Bergevin et al., 2017). The ear exhibits remarkable sensitivity, frequency selectivity, and dynamic range. For example, the human ear is sensitive to sound waves ranging from 20 - 20,000 Hz, spanning over six orders of magnitude in sound pressure level. Giving the ability to hear and distinguish a wide variety of sounds (loud screams and quiet whispers, high and low-pitched tones). Even untrained individuals can distinguish two tones differing in frequency by 0.5% (Hudspeth et. al, 2008). The ear's sensitivity is further highlighted by its ability to detect sounds at the energy level that approaches the thermal noise level in the inner ear, meaning that it induces displacement as small as the amplitude of motion due to thermal fluctuations in surrounding fluid (Hudspeth, 2014). This extraordinary sensitivity depends on the presence of an active process within the ear, which is responsible for amplifying a low-intensity incoming signal to overcome dampening (Gold, 1948).

In addition to detecting incoming sound, the healthy ear is also capable of emitting faint sound, known as otoacoustic emissions (OAEs). A portion of vibratory energy generated in the inner ear is emitted through the middle ear into the outside world and can thus be measured near the eardrum by using a sensitive microphone. Analysing OAEs we can see that this oscillatory energy is gathered at particular frequencies. The presence of OAEs provides valuable insights into the study of auditory biomechanics. OAEs can be categorized into two types: evoked otoacoustic emissions (eOAEs) and spontaneous otoacoustic emissions (SOAEs). Evoked otoacoustic emissions are generated in response to external acoustic stimuli, such as clicks or tones, that are presented to the ear. In

contrary SOAEs arise spontaneously in a quiet environment without external stimulation (by the quiet environment, we mean the absence of the external acoustic stimuli that are required for the eOAE generation). Among different types of otoacoustic emissions (OAEs), spontaneous otoacoustic emissions (SOAEs) are considered relatively simple to measure and require fewer assumptions for explanation. However, they are less commonly reported compared to other OAE types. In this research, we are interested in SOAEs and the mechanism of their generation in lizard ears.

Those spontaneous emissions are considered to be evidence that there is in fact an active process, mentioned before, taking place inside the inner ear. By "active", we mean some sort of metabolic-based process that creates power amplification. This process involves a nonlinear amplification mechanism (also often referred to as reverse transduction, or electro-mechano transduction) which enhances the detection of low-level sounds and compresses a wide range of sound intensities into a narrower range of vibration magnitude (Hudspeth, 2008). OAEs are generally considered a by-product of this active a process. And they are mostly attributed as arising due to the collective response of the hair cells. However, a detailed understanding of the underlying mechanisms still remains unclear.

Both spontaneous and evoked OAEs are clearly present not only in mammalian ears but also in a wide range of vertebrate ears (Bergevin et. al, 2015). Different classes are proven to have SOAEs, despite variations in inner ear morphology. Overall, most ears exhibit several relatively sharp peaks in their power spectra. At first look, both SOAE spectra and functionality of the ears within a species are similar (universal), but at the same time, there are idiosyncratic differences. An example of such is the fact that each ear exhibits a unique set of SOAE peaks and valleys. And within that spectra, each peak is characterized by its unique height and width. Thus, we can consider a number of peaks, their location, height and width as factors that determine/characterize each SOAE spectra. In the previous studies (Fruth et al., 2014, Wit et al., 2020) it has been shown that the irregularities in active term (parameter responsible for the self-sustained nature of a given oscillator, bifurcation parameter ϵ_j) affect on simulated spectra, leading to the formation of new spectral patterns. Their rationale is that the irregular active term distribution is due to irregularities in the developmental process. Such can be modeled by adding "roughness" (fixed irregularities) to distribution. At the same time, this is just an assumption (as we don't know for sure if the hair cell acts as a limit-cycle oscillator) and the possible distribution as well as the approximate value of the active term are still unknown. The term roughness itself is commonly used to determine irregularities in a frequency distribution. One might argue, that roughness in the tonotopic map rises from roughness in hair bundle height, as we think of it in passive consideration (depending on

mass and stiffness; and as a result on height). In this case, roughness in height distribution would lead to roughness not only in the tonotopic map but in other resulting parameters (see Section 3.2.1). However, in previous research (Vilfan and Duke, 2008, Wit et al., 2020; etc.) mostly it has been studied not in the way of tying the unique morphology to the idiosyncratic SOAE spectra. Also, we need to account for the fact, that hair cells in the ear are organized in rows of n hair cells (see Section 1.2.1). It has been shown before that hair cells within a row might be of the same height or frequency (Turner 1986; Shera, 2015; Negandhi et al., 2018). As such, forming a "step-like" distribution. All of these, are important objectives in our research as we aim to model a collective dynamic of the lizard's inner ear and to develop a realistic anole-inspired model of SOAE generation.

Hair cells are subject to many external and internal perturbations, at the same time the system is relatively stable to those (for example, SOAE spectral peaks return quickly after cessation of external forces). No matter what external forces were present in the ear beforehand in the absence of those it would return to its previous spontaneous activity, such that those "initial conditions" are irrelevant in this case. But it doesn't mean that we need to ignore the presence of those perturbations. We need to remember that hair cells are subject to noise, whether of thermal or acoustic origin. Additive noise has been already introduced to the models of SOAE generation (Vilfan and Duke, 2008; Wit et al.,2020; etc.) and it led to wider simulated peaks. But those studies were lacking on rationales and explanations for why peaks are broadening. One possible explanation can be that noise, either intrinsic (e.g., thermal agitation) or external, can cause perturbations and affect synchronization characteristics (leading to synchronization/cluster frequency fluctuations).

SOAEs provide powerful and noninvasive means to study the function of the inner ear (Bergevin et. al, 2015). Despite a variety of studies since the discovery of OAEs, there are still many open questions making the physics of hearing an active area of research. The inner ear is subject to many sorts of randomness ("initial conditions", noise and roughnesses forming unique tonotopic map and/or hair bundle height distribution) and their effect on the formation of unique spectra and peaks is yet to be studied. Based on everything that has been stated above, in our research, we aim to study the role of that randomness in the system and its effect on the process of SOAE generation.

1.2 Lizard Ears

As we already mentioned our interest in lizard ears, it is worth stating that they are a useful model for the study of inner ear biomechanics. One of the reasons is that

lizards have relatively simpler ears compared to mammals. To be able to model inner ear dynamics and fully understand underlying mechanisms, knowledge about its anatomy is required. Thus, in this section, we will cover the basis of lizard's inner ear morphology as well as the lizard's SOAEs.

In our research, we are focusing on Green Anole's (Anolis carolinensis) ears, but for comparative reasons (compare ears with free-standing hair cells and with salletal hair cells), we are also going to look into Tokay Gecko's (Gecko Gecko) ears.

1.2.1 Morphology

The auditory sensory organ of lizards is the basilar papilla, a narrow strip of epithelial cells (hair cells), that rests upon the basilar membrane, a sheet of connective tissue suspended from the limbic cartilages and separating the scala media from the scala tympani. The basilar papilla in lizards exhibits a tonotopic organization, with hair cells that respond to high-frequency located at one end and low-frequency-responsive hair cells at the other end. The exponential tonotopic map and the location of high-frequency hair cells at the papilla's apex are common to most lizards (Manley et al., 1999). Although, we usually assume a tonotopic map to be strictly exponential, one might argue that there may be various inconsistencies in that distribution (Turner 1986; Shera, 2015; Fettiplace, 2023).

The basilar papilla, the auditory sensory organ in lizards, exhibits remarkable diversity in its structure compared to other vertebrates (Manley and Köppl, 2008). Thus, let us look into the morphology of Green Anole and Tokay Gecko, as mentioned previously. As two of these lizards represent freestanding (Anole) and salletal (Gecko) hair cell structures, both types of hair cells play a role in modeling perspective in further chapters.

1.2.1.1 Anole

The anole basilar papilla has a length of around 0.4 mm and a width of around 0.1 mm. This compact sensory organ contains approximately 150 hair cells with a complex/unique arrangement (Miller, 1981; Negandhi et al.,2018). As mentioned above Anoles basilar papilla has a free-standing hair cell structure, meaning that it lacks an overlying tectorial membrane over the SOAE-producing cells (Negandhi et al., 2018). The arrangement of the hair cells within the basilar papilla of Anoles follows a specific pattern, also referred to as a "fingerprint" due to its uniqueness. So hair cells are organized into rows and each row contains approximately 4 hair cells. Notably, each hair cell has a bundle of approximately 50 stereocilia (Negandhi et.al, 2018). Within a row hair cell bundles are

oriented in a self-opposing fashion (Bergevin et al., 2015), meaning that the length of stereocilia gradually increases from the outer edges towards the midline of the papilla. Additionally, bundle height increases from 10 μm to 40 μm in the ventral direction (Figure 1.1). We acknowledge that there is a lack of precise specifications regarding how the height of hair cell bundles changes across these boundaries. As there is no direct study on the hair cell bundle height distribution for Anole ears, thus we might use studies done on other iguanids (Turner, 1986) as a reference for our assumptions on height distribution. Additionally, Negandhi et al. (2018) concluded that the progression in stereocilia length along the papilla is not strictly linear and there appear to be sectional changes which is consistent with measurements in other iguanids (Turner, 1986).

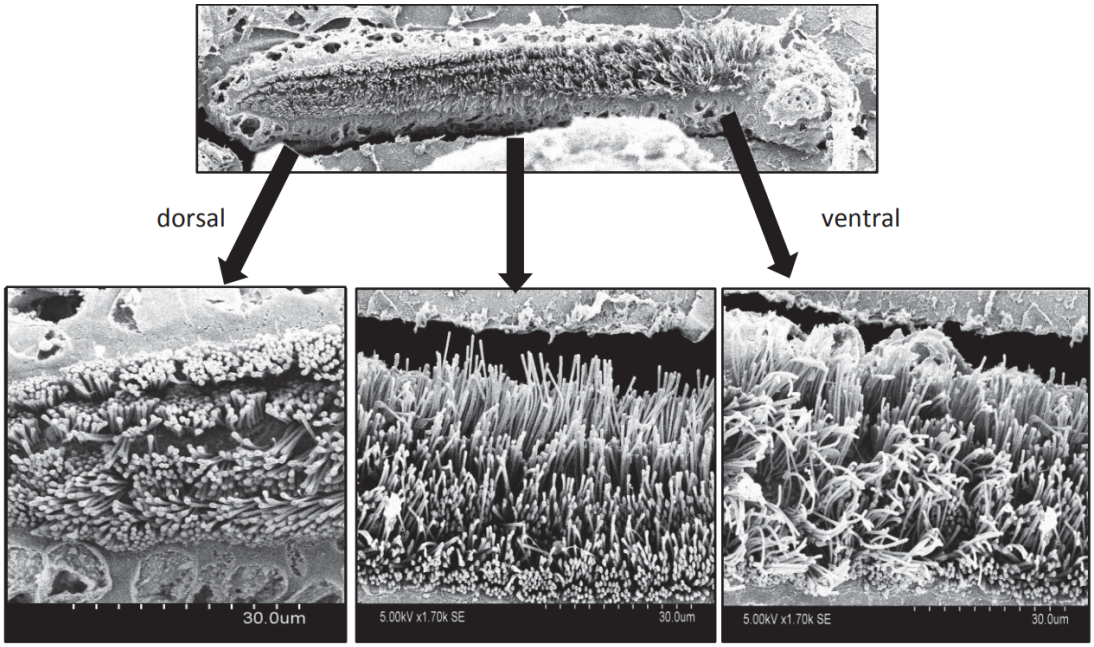

Figure 1.1: The Anole basilar papilla. Changes in hair cell stereocilia along the basilar papilla. [Negandhi et.al, 2018, Figure 3]

1.2.1.2 Gecko

The gecko basilar papilla has a length of around 2 mm and a width in between 0.05 and 0.13 mm and contains approximately 2000 hair cells arranged in about 240 irregular transverse rows (Miller, 1973; Gelfand et al., 2010). Above the papilla lie a continuous tectorial membrane and an array of about 170 sallets, a discrete tectorial structure about 20 mm in height (Figure 1.2 A). On the abneural side of the papilla, each sallet covers approximately 5-6 hair cells (Figure 1.2 B).

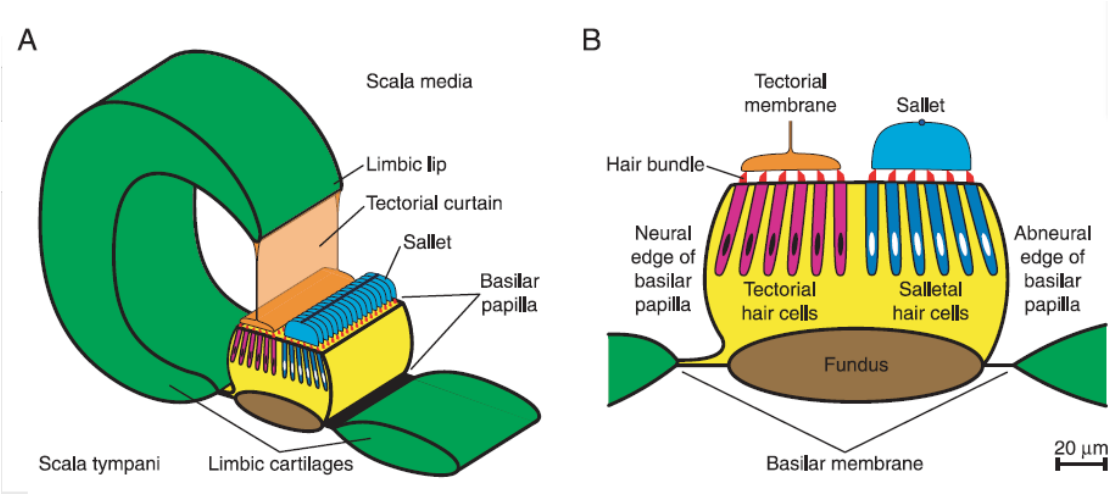

Figure 1.2: The Gecko basilar papilla. [Adapted from Figure 1, Gelfand et al., 2010]

1.2.2 SOAE

As previously mentioned, there have been numerous studies that examined non-mammalian SOAEs. Lizards, in particular, have been studied in this regard, as a group in which SOAEs are unusually common and demonstrate systematic variations corresponding to the structure of the inner ear (Köppl, 1995; Manley, 1997). As we have already covered the structure of the lizard's inner ear in the previous section, let us now look into the topic of the lizard's spontaneous otoacoustic emissions.

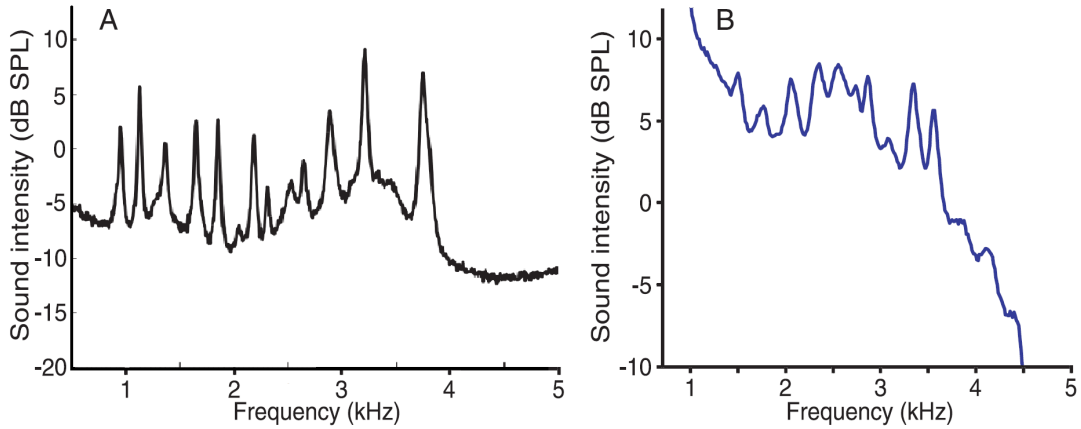

Figure 1.3: A. SOAE spectra from Anole; B. SOAE spectra from Gecko [Adapted from Figure 7, Bergevin et al., 2017 and Figure 1, Gelfand et al., 2010]

Lizards show SOAE activity, usually observed as a peaky pattern above the microphone noise floor. It is worth noting that while most ears exhibit SOAEs, there are some

cases where spontaneous emissions are not observed, although this occurrence is rare. Thus in the majority of ears, there can be distinguished from the background at least one or more prominent spectral peaks (even as many as 12 depending on the way peaks are determined). A specific region is identified as being an SOAE peak depending on its height and width, as well as sensitivity to temperature changes, and suppressibility by external tones. These peaks are usually located at a range of frequencies that the ear is most sensitive to. In the case of both Green Anole and Tokay Gecko, SOAE peaks are typically observed at frequencies around 1 and 5-6 kHz, as shown in Figure 1.3 (Bergevin et al., 2015; Gelfand et al., 2010).

1.3 Oustanding Questions

To further set the stage for this thesis, here is a short summary of what has been discussed above: OAEs are faint sounds emitted by the ear and measured by the sensitive microphone. They provide a non-invasive way to study the physiology of inner ear function, as they are generated by the hair cells. OAEs are divided into two basic types: SOAEs (arising in the absence of external sound) and eOAEs (in response to a stimulus). Lizards have a high occurrence of SOAEs, with systematic variations corresponding to the structure of their inner ear. Thus even for the same type of lizard, each individual lizard's ear exhibits a unique SOAE spectrum, characterized by a distinct set of peaks and valleys, as shown in Figure 1.4. Moreover, within these spectra, a given peak has its own unique characteristics such as height, width etc. These peaks demonstrate noticeable peak broadening compared to spectral peaks of other species (Bergevin et al., 2017). At the same time, ears are subject to randomness on different levels, such as unique patterns of the tonotopic map ("fingerprint"), internal fluctuations, thermal noise etc.

In our research, we are focusing on following some of the open questions in the field:

- How do hair cells work together to generate OAEs? Thus, our primary objective is to model a collective dynamic of the lizard‘s inner ear.

- Why spectral peaks are unique to a given ear? We aim to study the effect of variations in parameters (such as characteristic frequency and active term) on the formation of unique spectra.

- What is responsible for spectral peak broadening? One possible explanation for spectral peak broadening (fluctuation in the synchronization frequency of a cluster) can be the system's interaction with noise (for example, hair cells exposed to thermal

noise). Thus another goal of this research is to characterize how SOAE generators interact with noise and the role of randomness in the system.

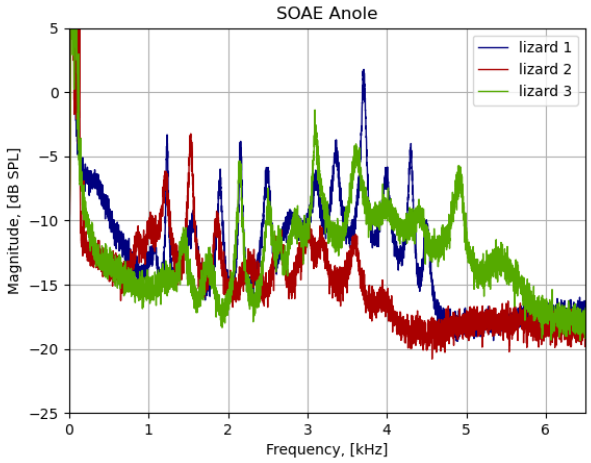

Figure 1.4: Comparison of SOAE activities from 3 different lizards (Green Anoles).

These (yet) unanswered questions, will be used as a guiding framework to structure the content of this research. By addressing these questions, we aim to contribute to the study of the underlying process behind SOAE generation and understanding of this subject matter.

1.4 Hypotheses

Based on the research objectives and outstanding questions stated above, we have formulated the following hypotheses:

- **Simulated spectra are relatively stable to perturbations (similarly to the way peaks in measured SOAEs show stability by quickly returning after discontinuing external force) and exhibit no sensitivity to initial conditions.**
- **Embedding roughness solely in the frequency distribution (i.e., modeling a unique tonotopic map) is sufficient to produce (stable) idiosyncratic spectra to a given simulated "ear".**
- **Embedding roughness in the distribution of hair bundle height (i.e., modeling morphological differences across individuals) is sufficient to produce (stable) idiosyncratic spectra to a given "ear."**

- **Broader peaks can be simulated by the inclusion of noise (either local or external/global), which causes interactions between clusters leading to frequency modulations (FMs).**

1.4.1 Additional Hypothesis

In case we need to reject the idea of modeling the inner ear as a chain of limit cycle oscillators, we also present an alternative model (for further information see Section2.1.4). This could potentially help to test the additional hypothesis that spontaneous oscillation can arise in the system of coupled non-limit cycle active nonlinear oscillators as a result of the system being noise-driven.

Chapter 2

Methods

2.1 Creating a Model

There have been numerous models of SOAE generation mechanism previously developed. Although those models share many elements, they differ widely in their details, featuring standing wave cavities (analogous to a laser), electric circuits, transmission lines, a single active limit-cycle oscillator, and systems of coupled limit-cycle oscillators etc (Zwicker, 1986; Wit, 1986; Zweig and Shera, 1995; Talmadge et al.,1998; Shera, 2003; Vilfan and Duke, 2008; Bergevin and Shera et al.; Epp et al.,2010; Gelfand et al., 2010; Ó Maoiléidigh, 2012; Wit et al, 2012; Fruth et al., 2014; Meaud, 2015). As the core of this research, we take Vilfan and Duke (2008) model. The Focus of this section is to review the logic behind creating a model of SOAE generation, as well as to review proposed model (Vilfan and Duke, 2008) and the potential variation to existing model.

When studying/modeling a phenomenon that occurs on both micro and macroscopic scales, it is essential to be specific about what scale we are focusing on. This choice often depends on questions that one wants to understand. In Case of inner ear dynamics, macromechanics refers to the motion of the basilar membrane and the cochlear partition as a whole, while micromechanics refers to the relative motion of hair bundles and of structures at the level of the reticular lamina and tectorial membrane. As we are interested in studying the underlying mechanism of SOAE occurrence via modeling the inner ear dynamic, our focus will be on the cellular level, specifically on inner ear hair cell (hair cell bundles) and their motion.

The further focus of this section is to review the logic behind creating a model of SOAE generation, as well as to review proposed model (Vilfan and Duke, 2008) and explore the potential variation or extensions to this model.

2.1.1 Hair Cell Bundle as Damped Harmonic Oscillator

As has been mentioned the ear is selective sensory system, it is capable of distinguishing and analyzing complex sounds by decomposing them into its frequency components. The unit responsible for that feature is hair cell (the core of our modeling), more specifically the hair cell bundle.

In response to incoming stimuli stereocilia bent, leading to the opening and closing of channels in the ionic membrane, modulating an ionic current. Thus, the hair cell is carrying information about oscillatory frequency. Additionally, the oscillating bundle is surrounded by fluids, which further influences its behavior. To capture these dynamics, the hair cell bundle is represented by a mass on the spring in the fluid. And described by the following equation of motion (Equation 2.1). Making in this case the hair cell bundle a damped harmonic oscillator with its characteristic frequency ($\omega = \sqrt{\frac{K}{M}}$).

$$\ddot{x} = -\gamma\dot{x} - \omega^2 x \tag{2.1}$$

This representation doesn't take into account the fact that the ear is active. It burns energy to reduce the effect of damping.

2.1.2 Hair Cell Bundle as Limit-Cycle Oscillator

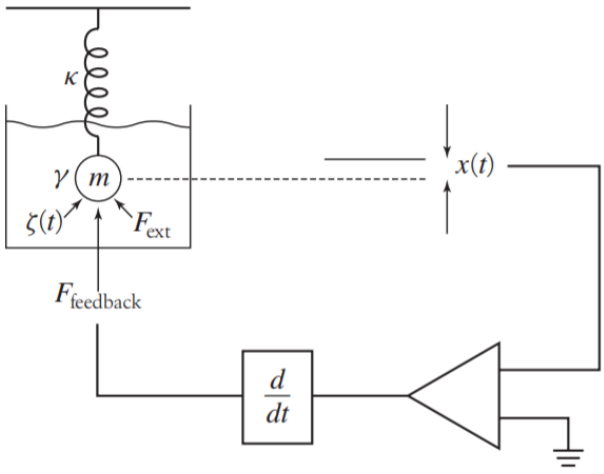

Figure 2.1: A schematic of active feedback. [Adapted from Bialek, 2012, Figure 4.52]

As stated before we need to account for the presence of an active mechanism. One way it can be done is by turning a hair cell into an active detector by introducing a feedback

force through the amplifier. This logic is proved by the fact that non-mammalian hair cell bundles in-vitro can behave as an active nonlinear system, or even as limit cycle oscillators (Crawford and Fettiplace, 1985; Martin and Hudspeth,1999; Ramunno-Johnson et al., 2009).

As depicted in Figure 2.1, as the model we now consider the mass on the spring that is moving through the surrounding fluid with the application of the feedback force generated by the amplifier. This feedback force introduces negative damping and nonlinearity to the system, enhancing the oscillatory behaviour of the hair cell bundle. Thus, the hair cell starts to act as a self-sustained oscillator, meaning it overcame damping and has limit-cycle oscillations. Such system can be described for example by the normal form equation for the supercritical Hopf bifurcation (Equation 2.2, where $z = x - \frac{i}{\omega}\dot{x}$) or the Van der Pol equation (Equation 2.3).

$$\dot{z} = i\omega z + \epsilon z - B|z|^2 z \tag{2.2}$$

$$\ddot{x} = \mu(1 - x^2)\dot{x} - \omega^2 x \tag{2.3}$$

2.1.3 Ear as Chain of Coupled Oscillators

The inner ear itself has a complex morphology, overall containing N (varies among species) hair cells. This leads us to the conclusion that the hair cell bundle (our active oscillator) does not exist on its own; it exists in the system. The fact that the number of peaks in the SOAE spectrum is much smaller than the number of hair cells (or sallets for geckos) suggests that the peaky nature of SOAE spectra might be due to the ongoing synchronization process between cells/sallets (Köppl and Manley, 1993). In this case, we need to consider cellular cooperativity and its effect on the inner ears dynamic. One way to explain cellular cooperativity is by introducing the formulation of coupled oscillators. One can divide coupling into two categories nearest neighbour and global. Let‘s look closer into the following models.

2.1.3.1 Nearest Neighbour Coupling

As a model, Vilfan and Duke (2008) used a chain of N-coupled non-linear, active limit-cycle oscillators. Coupling is such that each hair cell bundle (sallet in the case of Geko or bobtail lizard) is coupled to its nearest neighbour. From the modeling prospective anole-like models will use hair cell as an oscillatory unit and gecko-like models − sallets.

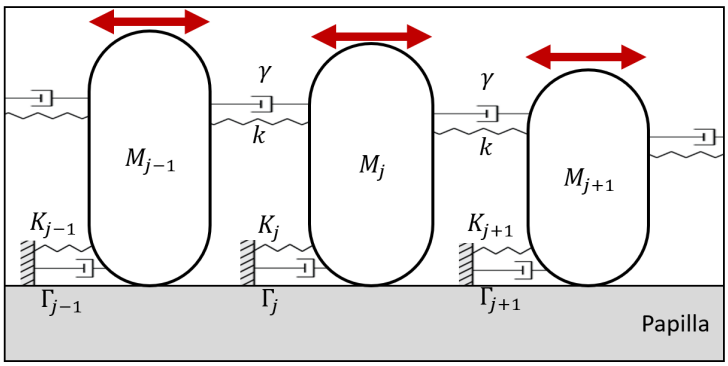

Figure 2.2: A schematic of nearest-neighbour coupling. [Adapted from Figure 1, Vilfan and Duke, 2008]

Each given hair cell bundle is represented as an active oscillator coupled to its nearest neighbours through elastic and damping elements (Figure 2.2). This model is described by Equation 2.4 (a detailed derivation of this equation is included in Appendix, Section A.2.1). The coupling force is represented by the therms $(id_I(z_{j+1}+z_{j-1}-2z_j)+d_R(z_{j+1}+z_{j-1}-2z_j))$, where d_I and d_R are imaginary (derives from elastic component k) and real components of the coupling term (derives from viscose component γ).

$$\begin{aligned}\dot{z}_j = {} & i\omega_j z_j + \epsilon_j z_j + id_I(z_{j+1}+z_{j-1}-2z_j) \\ & + d_R(z_{j+1}+z_{j-1}-2z_j) + \tilde{\xi}_j(t) - B|z_j|^2 z_j\end{aligned} \tag{2.4}$$

The idea of N active oscillators connected in a chain with nearest neighbour coupling is not limited by only Hopf oscillators (Vilfan and Duke, 2008). It can be extended to a system of Van der Pol oscillators (Gelfand et al., 2010) and be presented by equation (2.5).

$$\ddot{x}_j = \mu_j(1-x_j^2)\dot{x}_j - \omega_j^2 x - k(x_{j+1}+x_{j-1}-xz_j) - \gamma(\dot{x}_{j+1}+\dot{x}_{j-1}-2\dot{x}_j) + \xi_j(t) \tag{2.5}$$

As a result of nearest neighbours coupling, oscillators tend to synchronize themselves within groups of oscillators that oscillate with the same frequency. Those are known as frequency clusters, meaning that we can refer to this synchronization as frequency clustering. For clarification purposes let's specify that frequency clustering is a form of partial synchronization in a coupled system, in which each oscillator synchronizes with one of several clusters. However, the way this clustering occurs depends on the way we define the system and its key parameter.

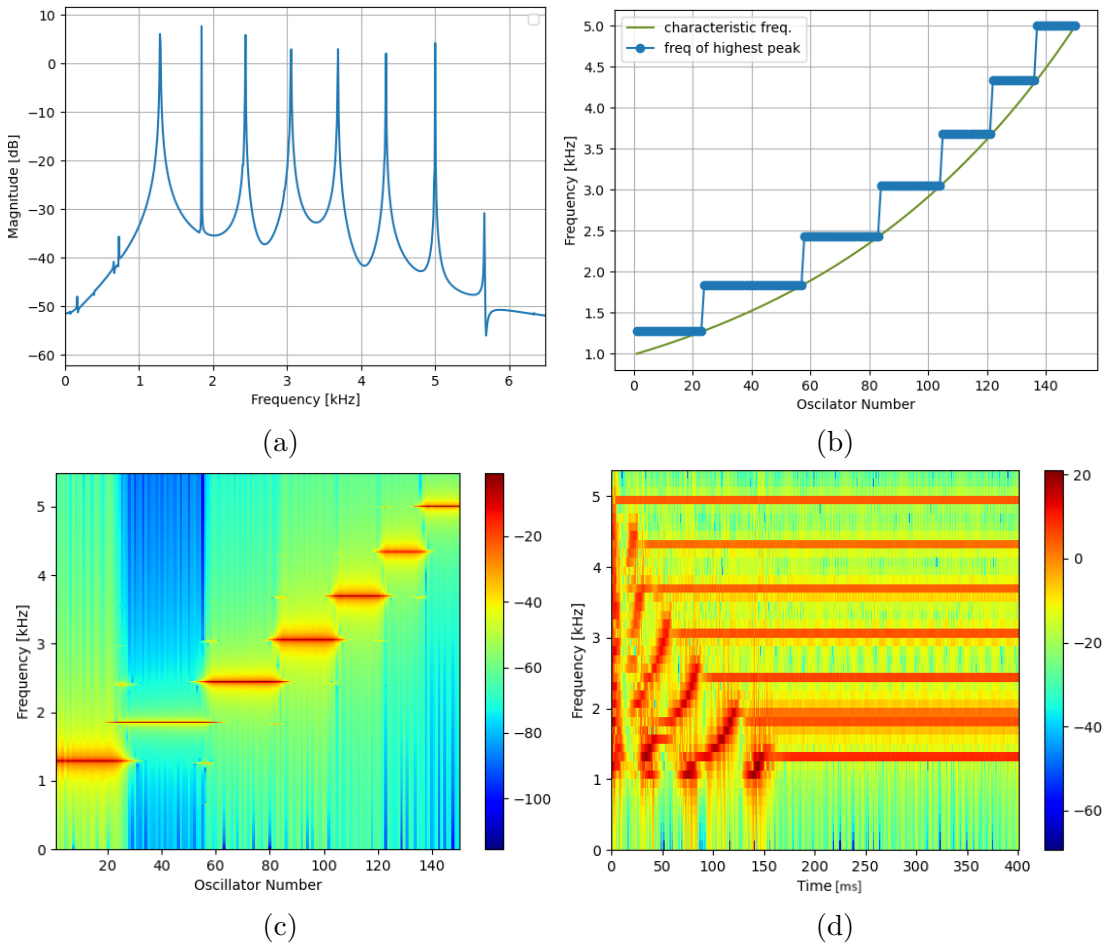

Figure 2.3: Chain with complex coupling and exponential frequency distribution. (a) Spectra; (b) clustering pattern, dominant frequency for each oscillator (frequency of the highest peak) compared to its natural frequency; (c) clustering heatmap; (d) spectrogram. Colorbar corresponds to the magnitude of spectra in dB.

In the model proposed by Vilfan and Duke (2008), frequency clustering can be observed. Figure 2.3 depicts the results model of 150 coupled oscillators. Oscillators have an exponential frequency distribution between $\omega_1 = 2\pi - \omega_N = 5 * 2\pi$, active term $\epsilon = 1$ and $B = 1$ are constant. For this simulation, we used constant coupling terms $d_R = 0.157$, $d_I = -1$. Thus, having the same parameters as Vilfan and Duke (2008) used in their simulations (Figure 4, Vilfan and Duke, 2008) except for the number of oscillators as we are interested in a system with 150 oscillators or more (as anole ear has approximately 150 hair cells and gecko ear has around 170 sallets). We clearly can see the occurrence of 7 clusters in subplots (b) and (d) and those frequencies correspond to peaks in spectra (subplot (a)). To determine the number of clusters and cluster frequency, for each oscillator we choose the frequency of the highest peak. We also can note that some oscillators contribute to more than one cluster, this phenomenon would be more noticeable in other

simulations included later. Thus, we find the more proper way to depict clustering via plotting spectra for each oscillator in the heatmap (Figure 2.3, subplot (c)), where colorbar indicates the magnitude in [dB]. It shows that for each oscillator frequencies from subplot (b) are just dominant ones. Thus, we still can see the clustering but also gain additional information (for example, how narrow the peak is, or whether the oscillator is "jumping" in between clusters). The spectrogram in subplot (d) proves that this system is able to reach a "steady state".

2.1.3.2 Global Coupling

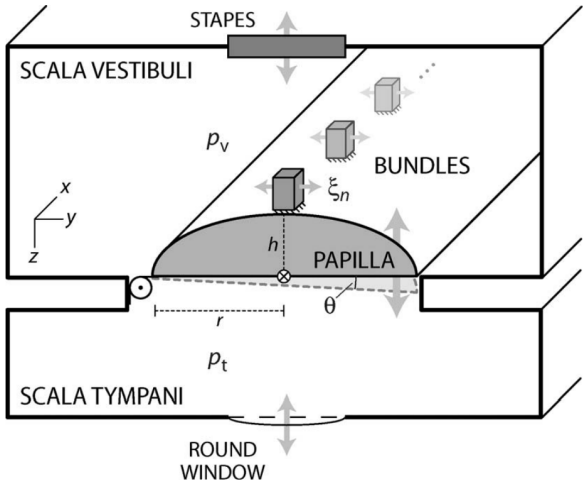

Figure 2.4: A schematic of global coupling. [Adapted from Figure 1, Bergevin and Shera, 2010]

To continue with the next model, we need to take into account the fact that hair cells are lying on top of the basilar papilla. This leads to the idea that besides nearest-neighbour a global coupling exists (Bergevin and Shera, 2010). By global coupling we mean each hair cell being connected to a basilar papilla which by itself acts as a damped harmonic oscillator.

Such a system is a modified version of Vilafan and Duke (2008) model with an additional oscillator (papilla represented by a damped harmonic oscillator, Figure 2.4) and additional coupling force F_{jp}. So now hair cell bundle can be described by Equation 2.6 and basilar papilla by Equation 2.7, where h_j is a height of the hair cell bundle and r_j − location relative pivotal side of the papilla (a derivation of this equation is included in

Appendix, Section A.2.2).

$$\begin{aligned}\dot{z}_j =& i\omega_j(z_j - \frac{1}{2}\frac{h_j}{r_j}z_p) + \epsilon_j z_j - \epsilon_{jp}\frac{\omega_p}{\omega_j}\frac{h_j}{r_j}z_p + id_I(z_{j+1} + z_{j-1} - 2z_j) \\ &+ d_R(z_{j+1} + z_{j-1} - z_j) + \tilde{\xi}_j(t) - B|z_j|^2 z_j\end{aligned} \tag{2.6}$$

$$\dot{z}_p = i\omega_p z_p + \epsilon_p z_p + \frac{M_j}{M_p}\sum[\frac{i}{2}\frac{{\omega_j}^2}{\omega_p}(z_j - z_p) - \epsilon_{jp}(\frac{\omega_j}{\omega_p}z_j - z_p)] \tag{2.7}$$

2.1.4 Hair Cell Bundle as Active Non-Limit-Cycle Oscillator

The key assumption underlying the models discussed above is that the hair cells can be represented as limit cycle oscillators. As mentioned before, the scientific proofs of that where observed only in-vitro. There might be suggestions for it as well as against it, as there isn't (yet) a proof that hair cell in fact oscillates spontaneously (in-vivo). The chain of limit cycle oscillators would still oscillate even if we turn off the coupling and noise. We would like to look into SOAEs as a by-product of noise-induced spontaneous activity of hair cells. Following the additional hypothesis from Section 1.4: spontaneous oscillation can arise in the system of coupled non-limit cycle active nonlinear oscillators as a result of the system being noise-driven.

In this case, the hair cell bundle can be still depicted by Figure 2.1, but in this case, damping would be reduced by nonlinearity and won't reach a negative value. So the hair cell is still active (it burns energy to reduce dumping) but does not oscillate on their own. One way that we can describe this model is by writing a nonlinearity as a Lorentzian-like "valley" in damping for small displacement (Equation 2.8), where d is depth, w is the half-width of half maximum of the "valley". And Equation 2.9 describes a chain of coupled active non-limit-cycle oscillators.

$$\ddot{x} = -(\gamma - d\frac{w^2}{x^2 + w^2})\dot{x} - \omega^2 x \tag{2.8}$$

$$\ddot{x}_j = -(\gamma - d\frac{w^2}{x^2 + w^2})\dot{x} - \omega^2 x - k(x_{j+1} + x_{j-1} - xz_j) - \gamma(\dot{x}_{j+1} + \dot{x}_{j-1} - 2\dot{x}_j) + \xi_j(t) \tag{2.9}$$

As by this time, despite our best effort, we didn't succeed on getting meaningful results while testing this hypothesis. As such this will be kept as an hypothesis that yet needs to be tested. Thus, whether spontaneous SOAE-like oscillation can be generated by a system of coupled non-limit cycle active nonlinear oscillators as a result of the system being noise-driven, is still an open question.

2.2 Numerical simulation

All simulations have been performed using Version 3.8 of Python. We represented models using an array of N (number of hair cells/sallets/oscillators) first-order ordinary differential equations. To obtain waveforms we used a built-in solver with adaptive stepsize *solve_ivp* and *complex_ode* from the *scipy.integrate* package, choosing the explicit Runge-Kutta method of order 5(4), RK45. For all simulations sampling rate (sampling frequency) was set at 128 kHz, while the number of time points (duration of waveform) varied depending on the specific simulation, and the purpose of that simulation (for example, for systems with the presence of noise we needed long waveforms to be able to conduct averaging and proper analysis). To obtain spectra we used $rfft$ from the *scipy.fft* package. For simulation duration timesaving reasons noise was interpolated using $interp1d$ and $interp2d$ from *scipy.interpolate* package (for further information see Section 2.4). Further analysis of specific peaks within a spectrum was done using preexisting code in the code library of our laboratory.

2.3 Parameters

In our model, we have two sets of parameters $(K_j, \Gamma_j, M_j, k, \gamma)$ and $(\omega_j, \epsilon_j, d_{Rj}, d_{Ij})$, let's refer to them as "primary" and "secondary" respectively. By using information about lizard's inner ear morphology (Section 1.2.1), physiology and mechanical properties of hair cells we are able to make some estimations of the system's parameters. These estimations allow us to incorporate more realistic values into a model.

2.3.1 Estimated Values

Anole. To estimate the mass of the hair cell bundle we assumed is as the one having a cylindrical shape. Therefore we used an equation $M_j = \rho h_j \pi \frac{d}{2}^2$, where d is the diameter of the bundle (approximately the same for all hair cell bundles $d = 10\mu m$), h_j is the height of bundle (largest stereocilia) (vary in the range $30\mu m - 10\mu m$). In this case for anole estimated oscillator mass would be with a range $2.4 * 10^{-12} - 0.8 * 10^{-12} kg$. We know that the expected frequency range is between 1-5 kHz. Using the equation $\omega_j^2 = \frac{K_j}{M_j}$ we can estimate that $2.4 * 4\pi^2 * 10^{-6} \frac{kg}{s^2} \leq K_j \leq 20 * 4\pi^2 * 10^{-6} \frac{kg}{s^2}$. We know that Hair bundle stiffness can be written $K_j = N_{Sj} \frac{1}{h_j{}^2} * K_{sr}$ where N_{Sj} is the number of stereocilia, K_{sr} is the rotational stiffness of single stereocilia (Crawford and Fettiplace, 1985). Based on Negandhi et.al we can assume that N_{Sj} is constant to some order and equals approximately 50, then $\frac{K_{150}}{K_1} = (\frac{h_1}{h_{150}})^2$ also making $(\frac{\omega_{150}}{\omega_1})^2 = (\frac{h_1}{h_{150}})^3$. We have

$\frac{K_{150}}{K_1} = 8.33$ and $\frac{h_1}{h_{150}} = 9$, $(\frac{\omega_{150}}{\omega_1})^2 = 25$ and $\frac{h_1}{h_{150}} = 27$ this suggests that N_{Sj} has a slight variation. For $N_{Sj} \approx 50$ we can estimate $K_{sr} \approx 0.2 * 10^{-14}$, which is 10 times more than the value at (Crawford and Fettiplace, 1985). On the other hand, we can assume that M_j can be written as $M_j = N_{Sj} M_s$ (if we don't account for differences in stereocilia height within the hair cell bundle), this suggests that these variations are coming from rotational stiffness of stereocilia.

Gecko. Fettiplace (2020) calculated the mass of the sallet as a mass of semicircular slice, diameter $40\mu m$, thickness $3\mu m$ and density 1000 $\frac{kg}{m^3}$, which relates to Gelfand's (2010) salletal width $50\mu m$, salletal height $20\mu m$ and density of the sallet is equal to the density of water, giving $M = 1.9 * 10^{-12} kg$. According to this information M_j – constant, which leads to the conclusion that characteristic frequency depends only on stiffness. Morphology suggests a low–high frequency gradient in stiffness because of a decrease in hair bundle height ($H = 16{-}4.6\mu m$), and increases in stereociliary complement (N_S = 32–48) and in numbers of bundles devoted to each sallet (N_{HB} = 4–8) giving $K_j = K_s * N_S * N_{HB}$, where $K_s = \frac{K_{sr}}{H^2}$ – stiffness of a single stereocilium and $K_{sr} = 0.026 * 10^{-14} \frac{N*m}{rad}$ – rotational stiffness of a single stereocilium (Fettiplace,2020). $\omega_j = \sqrt{\frac{K_j}{M_j}}$ can be rewritten as $\omega_j = \sqrt{\frac{K_{sr} * N_S * N_{HB}}{H^2 M_j}}$. Using equation for ω_j, we can get $\omega_1 \approx 1.3 * 2\pi * 10^3 \frac{rad}{s}$, $\omega_N \approx 7.9 * 2\pi * 10^3 \frac{rad}{s}$ and for $N_{HB} = 6$ $\omega_1 \approx 1.6 * 2\pi * 10^3 \frac{rad}{s}$, $\omega_N \approx 6.8 * 2\pi * 10^3 \frac{rad}{s}$, it is similar range and extent to those observed experimentally (1–5 kHz).

Based on observation of exponential tonotopic map in lizards (Manley et al., 1999), for our numerical simulation we are going to use values of K_j and ω_j with exponential distribution for both Anole and Gecko. M_j with exponential distribution for Anole and constant for Gecko. We are assuming that $K_{sr} * N_{Sj}$ varies such that $\omega_j^2 = \frac{K_j}{M_j}$. It is important to state that those distributions might change for Hyphotesis 3 and all changes would be discussed in the corresponding chapter. Parameter Γ_j (as well as ϵ_j) includes two terms damping of the bundle and negative damping that comes from feedback force (active process), it still hasn't been proven that hair cells behave as limit cycle oscillators, so we are not able to compare a second part of this parameter to some measured value. Primary parameters k, γ and the secondary d_{Rj}, d_{Ij} determine the coupling terms of the system. For most of the simulations, we are going to use the same values for Γ_j, d_{Rj}, d_{Ij} as Vilfan and Duke (2008) used.

2.3.2 Scaling and Order Correction

For simplicity in our research, we are going to use the $[kHz]$ scale, which requires us to rewrite other parameters using $[ms]$ instead of $[s]$. Table 2.1 includes both "primary"

and "secondary" parameters, their values for Anole and Gecko, sign, rescaled order and whether the parameter is constant or varies across a chain of oscillators. To calculate order Γ_j, γ and k, the assumption that ϵ_j, d_I and d_R have 10^0 order correspond to parameters chosen by Vilfan and Duke (2008). Parameters that have blank spaces in the value column are parameters that will differ for simulation, as we couldn't connect them to actual measurements. A question mark means that we don't know for sure if this parameter is constant or not.

	equation	value (anole)	value (gecko)	sign	rescaled order	constant
ω_1	$\sqrt{\frac{K_1}{M_1}}$	$1 * 2\pi * 10^3$	$1 * 2\pi * 10^3$	$+$	10^0	$-$
ω_N	$\sqrt{\frac{K_N}{M_N}}$	$5 * 2\pi * 10^3$	$5 * 2\pi * 10^3$	$+$	10^0	$-$
M_1	$-$	$2.4 * 10^{-12}$	$1.9 * 10^{-12}$	$+$	10^{-12}	$-$
M_N	$-$	$0.8 * 10^{-12}$	$1.9 * 10^{-12}$	$+$	$10^{-13} - 10^{-12}$	$-$
K_1	$-$	$9.5 * 10^{-5}$	$7.5 * 10^{-5}$	$+$	10^{-11}	$-$
K_N	$-$	$7.9 * 10^{-4}$	$18.8 * 10^{-4}$	$+$	$10^{-10} - 10^{-9}$	$-$
ϵ_j	$-\frac{\Gamma_j}{2M_j}$			$+$	10^0	?
d_R	$\frac{1}{2}\frac{\gamma}{M_j}$			$+$	10^0	v(anole) c(gecko)
d_I	$-\frac{1}{2}\frac{k}{\sqrt{K_j M_j}}$			$-$	10^0	varies
Γ_j	$-$			$-$	10^{-12}	?
γ	$-$			?	10^{-12}	constant
k	$-$			$+$	$10^{-10} - 10^{-9}$	constant

Table 2.1: Parameters, estimated values and order

2.3.3 Variable Parameters

As has been stated before this system depends on two sets of parameters and equations in the second column of Table 2.1 highlight the relationship between these two sets (also see equations A.6−A.9). As we can see all of the "secondary" parameters depend on M_j, also both ω_j and d_{Ij} depend on K_j as well. Let's consider the fact that we have a system of oscillators with a frequency distribution which means that the ratio K_j/M_j varies across the chain. For the anole-like model, each hair cell has its unique mass and stiffness whereas, for the gecko-like model, we can assume that all sallets have the same mass and each sallet has unique stiffness. This suggests that at least d_{Kj} and d_{Ij} vary across a chain for anole and at least d_{Ij} for gecko (in this case, we cannot ignore

determining whether ϵ_j is the same for all oscillators as it depends on Γ_j which is still a purely intuitive parameter). In their research, Vilfan and Duke (2008) model a bobtail lizard's inner ear (salletal structure) and introduce a distribution only for frequencies, but this assumption leads to a violation of Newton's Third Law. The goal of this subsection is to compare results from systems with constant parameters and variable parameters (with distribution across a chain of oscillators) for both anole-like and gecko-like models.

2.3.3.1 Results for Gecko-like Model

Only reactive coupling d_I varies. Even with the assumption that the mass of the oscillator does not change within the chain (sallet of constant mass) reactive coupling d_I would vary due to changes in the spring constant. To compare how this correction could affect systems synchronization, let us take a look at four possible scenarios: (1) d_I is the same for all oscillators (Vilfan and Duke, 2008), (2) d_I varies such that the first oscillator has the same value as in the first scenario, (3) d_I varies such that oscillator in the middle has the same value as in the first scenario, (4) d_I varies such that the last oscillator has the same value as in the first scenario. The effect of different scenarios on system clustering and spectra are shown in Figure 2.5. We simulated a system of 150 oscillators for these 4 scenarios of d_{Ij} distribution, with the rest of the parameters being the same as for Figure 2.3.

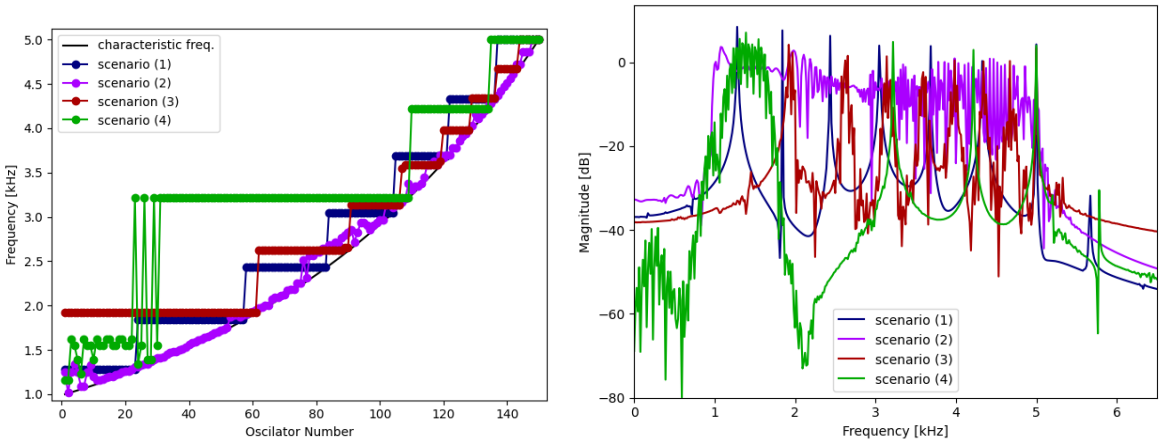

(a) (b)

Figure 2.5: (a) Clustering patterns, dominant frequency for each oscillator for each scenario. (b) Spectra of the system for 4 possible scenarios. Where $d_{I1} = d_{Ij} = d_{I150} = -1$ − blue, $d_{I1} = -1$ − purple, $d_{I75} = -1$ − red and $d_{I150} = -1$ − green.

In scenario (2), where $d_{I1} = -1$, the coupling is too weak. Thus, the system fails to synchronize, resulting in a lack of peaky structure of systems spectra. In scenarios (3)

and (4), we see that stronger coupling leads to synchronization into bigger clusters. The smaller the characteristic frequency is, the smaller the frequency difference ($\Delta\omega$) and the stronger clustering which boosts an inequality in the number of oscillators per cluster for an exponential tonotopic map. An interesting outcome gives us a scenario (3), where $d_{I150} = -1$. We see wider peaks due to declustering in areas of low frequency. This is not the peak broadening that we expect, as we still see a clear superposition of peaks at all those frequencies, but it might be of interest to us to study noise driven version of this scenario. Although we see clustering occurring for the gecko-like model if we would compare these results to the one of constant parameters (red and blue line), we see the inconsistency between them. Thus, if we would want to model a gecko ear we need to account for stiffness distribution that makes an imaginary component of the coupling term vary across oscillators.

2.3.3.2 Results for Anole-like Model

Spring constant K_j ***and mass*** M_j ***vary.*** To analyze differences in results between Vilfan and Duke's (2008) model and the anole-like model, in the same manner, as for the gecko-like model, we are going to compare 4 different scenarios. As has been stated above most of the parameters in the case of anoles ear are going to vary across a chain. To compare how this correction could affect systems synchronization, we introduce these scenarios: Scenario (1) is the same; Scenario (2) $-$ k and γ are chosen such that $d_{I1} = -1$ and $d_{R1} = 0.157$; Scenario (3) $-$ $d_{I75} = -1$ and $d_{R75} = 0.157$; Scenario (4) $-$ $d_{I150} = -1$ and $d_{R150} = 0.157$. We simulated a system of 150 oscillators for these 4 scenarios of d_{Ij} and d_{Rj} distributions, with the rest of the parameters being the same as for Figure 2.3.

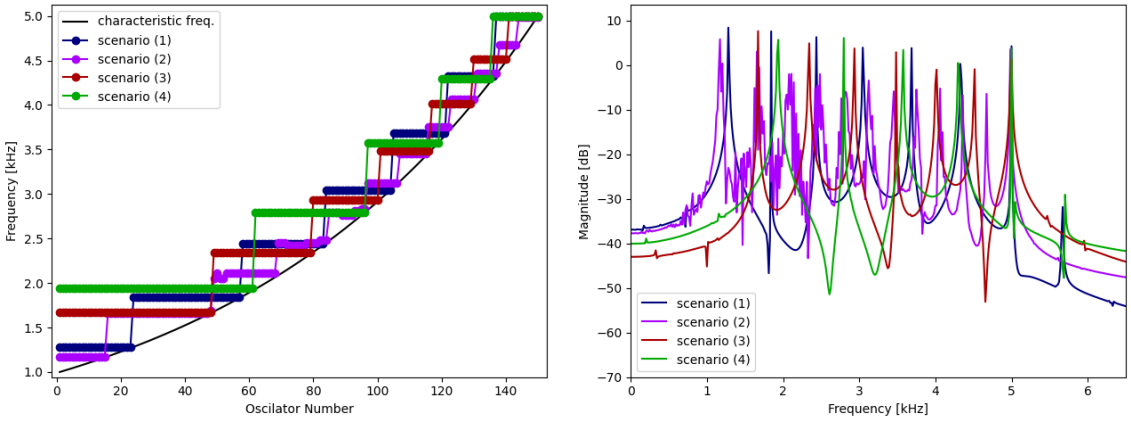

(a) (b)

Figure 2.6: (a) Clustering patterns, dominant frequency for each oscillator for each scenario. (b) Spectra of the system for 4 possible scenarios.

In all of these scenarios, the introduction of mass and stiffness distribution led to new clustering patterns. And as expected we see as coupling increases synchronization gets stronger and clusters become larger. Also for scenario (2) we see that a few oscillators are desynchronized, leading to some sort of peak broadening by adding energy at those frequencies. Comparing results for different scenarios we can conclude that changes in the strength of coupling terms k and γ (or d_I and d_R as a result) lead to new clustering patterns. This statement leads to new thoughts on how "different ears" (different sets of spectral peaks and valleys) could be generated. Even though we see that the oscillators in an anole-like model tend to synchronize within clusters, those clustering patterns are different from the one observed in the model with constant parameters (blue line). Thus, if we would want to model a anole ear we need to account for height distribution, which results in mass and stiffness and this eventually affects "secondary parameters".

2.4 Noise Introduction

In our research we recognize the significance of noise and its influence on the dynamics of the system. As we stated before (Section 1.4) the noise might introduce fluctuations to the frequency of an individual oscillator (meaning fluctuations in the synchronization frequency of the cluster). Thus, there is an importance in introducing noise to the system. We simulated the effect of noise by adding an additional term $\tilde{\xi}_j(t)$ as you can see in Equation 2.4.

$$\begin{aligned} \dot{z}_j = i\omega_j z_j + \epsilon_j z_j + id_I(z_{j+1} + z_{j-1} - 2z_j) \\ + d_R(z_{j+1} + z_{j-1} - 2z_j) + \tilde{\xi}_j(t) - B|z_j|^2 z_j \end{aligned} \tag{2.4}$$

As we use built-in functions (*solve_ivp* or *complex_ode*) to solve our ODEs and both of them are using an adaptive step size. This means that simply generating a random noise value for each run (inside a solver) can significantly slow down our simulation. As we observed that in some cases runtime was up to 50 times slower than for the noiseless system. To address this issue and optimize the simulation time, we use interpolation while introducing noise needs to the system. A noise array was then created by randomly selecting a new value from a normal distribution with a sample rate the same as for the waveform. In this way, we generated a "noisy pattern" which we can now turn into a function by interpolating it. It is worth mentioning that the idea of generating a noisy pattern will be used in this research not only for the noise term itself but for any randomness introduced to the system.

Chapter 3

Hypothesis 1

Simulated spectra are relatively stable to perturbations (similarly to the way peaks in measured SOAEs show stability by quickly returning after discontinuing external force) and exhibit no sensitivity to initial conditions.

We determine SOAEs as faint sounds emitted by the ear in the absence of external force. This is not the ideal explanation because, in the living system, we won't be able to achieve these conditions when there aren't any external forces that act on the system. Although hair cells are relatively stable even when subject to many external and internal perturbations, it doesn‘t mean that we ignore their presence. An example of stability could be the fact that SOAE spectral peaks return quickly after cessation of external forces, or that the SOAE spectrum of a given ear is consistent across different measurements at the same conditions. In other words, the SOAE generation process is not sensitive to any forces that have been acting on the system before the conditions to measure spontaneous activity were achieved. In our simulations, we first start a spontaneous oscillatory activity by considering the part of the waveform where the system reached its "steady state". Thus we hypothesize that initial conditions should be irrelevant in this case (in our simulation as initial conditions we use initial values for displacement and velocity of hair cell, but also could be any other force that pushed the system from equilibrium). To test that we would simulate a system with the same parameters but different initial conditions. As a part of this hypothesis, we also assume that after presenting a force for a short period of time our simulated system needs to return back to the same "steady state", which could easily be tested. It is worth mentioning that we are not presently quantifying such sensitivity (e.g., Lyapunov exponents).

3.1 Results

As we expected, both Vilfan and Duke-like (constant parameters for 150 hair cells) and the "anole-like" models show no sensitivity to the initial condition (x_0 and $\dot{x}_0$). Figure 3.1 subplot(a) shows that peaks remained at the exact same location and the only variations were in the valley region. At the same time for this analysis during each trial for a short period of time ($\approx 50\ ms$) we added a sinusoidal force with amplitude 3 and frequency 3 kHz (Figure 3.1 subplot(a)). The spectrogram depicts that the system first synchronized to its "steady state" resulting in 5 peaks and as we turned on the force it entrained oscillators (plateau at 3 kHz). Then peaks returned after discontinuing force after a short period of time ($\approx 200\ ms$). The same results were achieved for the model with constant parameter distribution. Thus, we can conclude that these models with those exact parameters are stable and are insensitive to changes in initial conditions.

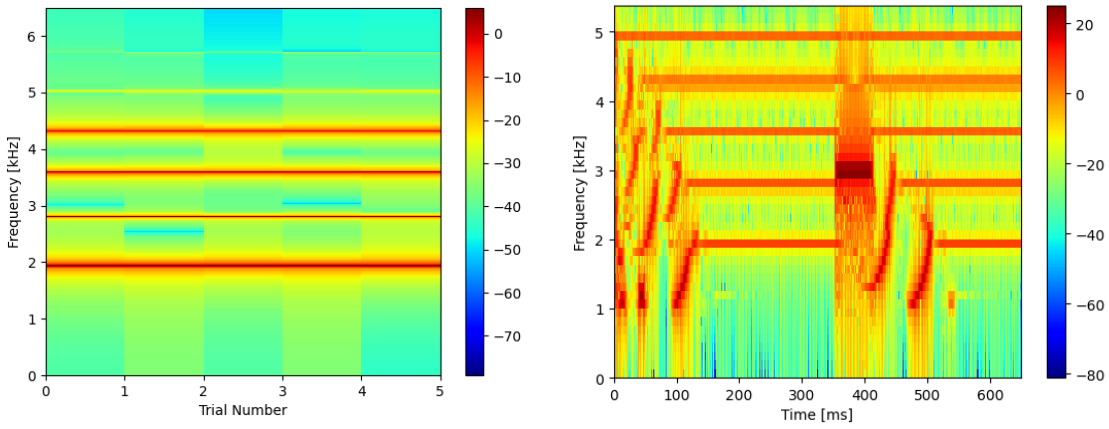

(a) (b)

Figure 3.1: (a) Heatmap representing spectra for "anole-like" system with different initial conditions. (b) Spectrogram of trial 5. Colorbar − magnitude [dB]

Although we didn't state the number of oscillators as a systems parameter, it has a crucial effect on the simulation outcome. Especially, as different types of lizards have variations in the number of hair cells and sallets (anoles have approximately 150 hair cells, while geckos and bobtail lizards have around 150 and 80 sallets, respectively), corresponding to a number of oscillators (Section 1.2.1). However, in the case of Anole, it all depends on the assumption that we are using while determining the system. At the same time, we need to keep in mind that this model was developed for ears with salletal hair cells, such that it could be translated into a $1-D$ array of coupled oscillators. If we continue to model anole inner ear as the one-dimensional chain of 150 coupled oscillators, then our system does not depend on initial conditions. At the same time, if we want to

account $2-D$ orientation of hair cells, the easiest way to model it is by assuming that hair cells in a row are already synchronized, such that we can assume that they are behaving as one oscillator.

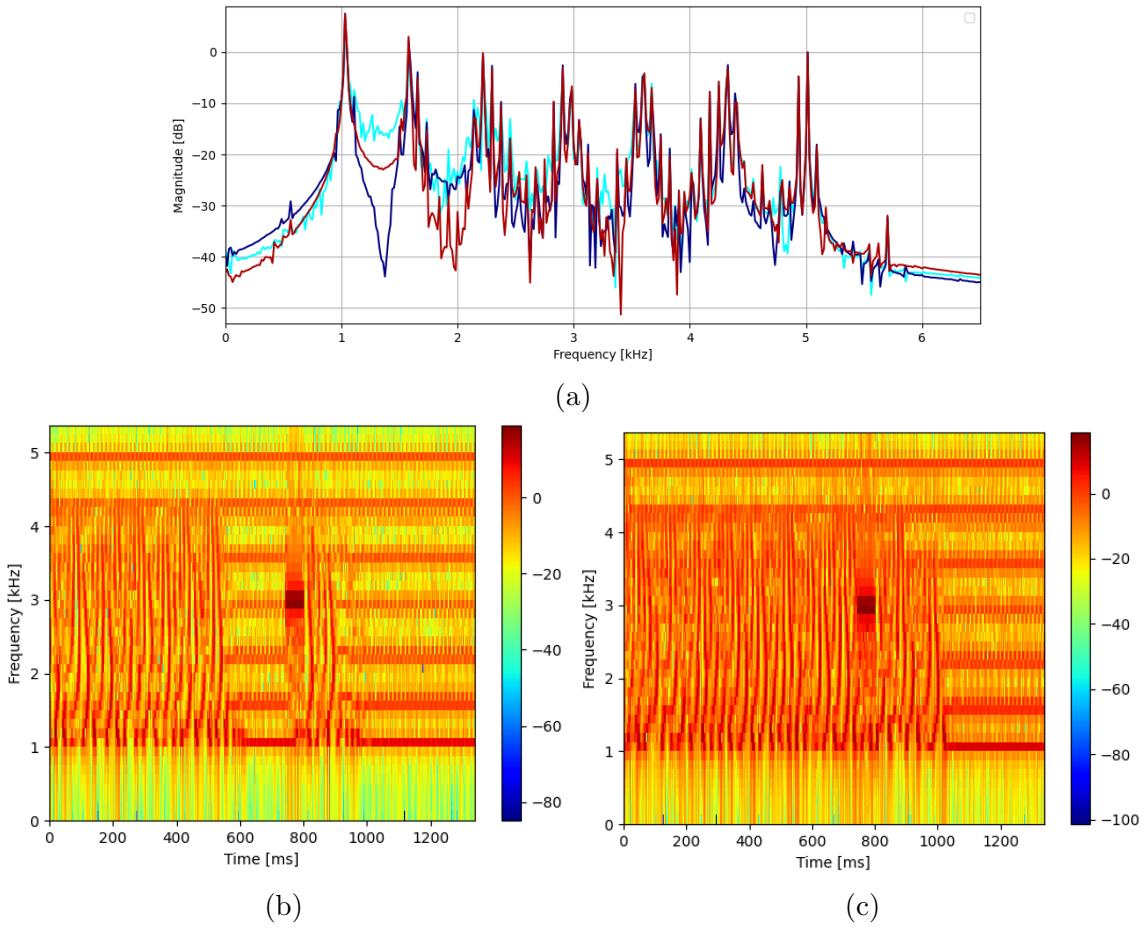

Figure 3.2: (a) Spectra for Vilfan and Duke (2008) system with 3 different sets of initial conditions. (b) Spectrogram of trial 7. (a) Spectrogram of trial 21. Colorbar − magnitude [dB]

As we already established, for large N ($N \geq 100$) dominant frequency distribution is insensitive to initial condition (x_0 and $\dot{x}_0$), we still can see some minor changes in the valley region of spectra. Therefore, for gecko ears outcome is independent of initial conditions. Contrary to Gecko the Bobtail lizard (Vilfan and Duke, 2008) has a smaller number of sallets. With the first trials, the system of 80 oscillators seems to be sensitive to changes in initial conditions. The key in this case is to extend the time we wait for the system to reach its "steady state", in this case, this time is relatively longer (from $x2 - x5$ longer) compared to the previous system and depends on a set of initial conditions. In most cases the system is synchronized and after the force is turned off returns to its

"steady state" Figure 3.2 (b). At the same time both scenarios, when the system wasn't synchronized and synchronized after discontinuing force, also occurred (see subfigure(b)). As for sensitivity to the initial condition, the situation is less clear. As spectral peaks contain a superposition of few sharp peaks (contrary to narrow peaks for 150 oscillators), in Figure 3.2 (a) we see minor changes to peak structure for different initial conditions. As for models with variable parameter distribution (see Section 2.3.3) system didn‘t reach a "steady state" and as a result is also unstable.

Using an alternative way to model an anole ear, by simulating a system of 38 oscillators, leads to the system not being able to synchronize into a "steady state". With given parameters system becomes sensitive to initial conditions and unstable. We could resolve this issue by increasing other parameters as the difference in characteristic frequency between two neighbouring oscillators increased, but this leads to a reduction in the number of peaks (clusters) to the critical scenario of only up to 3 peaks.

3.2 Discussion

As has been stated above, the number of oscillators has a crucial effect on the simulation outcome. By changing the number of oscillators in a chain we are changing the $\Delta\omega$ between two neighbouring oscillators, which changes the proportions in between all parameters. Thus, the sensitivity to changes in initial conditions are by increasing the active term and coupling, which eventually leads to fewer clusters. A proper analytical estimation of what those parameters are for this model can then be performed. It is worth mentioning that there aren't any measured estimations as to what those parameters should be, as this parameter relies on the assumption that hair cells are in fact oscillating spontaneously and behave as limit cycle oscillators. However, we are not interested in systems that consume even more energy and result in spectra with 1 or 2 peaks on the higher end of the chain. We also want our model to be able to synchronize into a stable "steady state" to mimic SOAEs. Thus, we either need to stick with large N or justify why this sensitivity can be ignored. One of the possible explanations might be the fact that in the actual ear, we don't know when the initial conditions were set, and when and if we can measure how the ear is synchronized from the initial condition to the "steady state". However, what can be measured is the stability of the steady state and how the ear recovers from the introduction of some sort of stimuli. Thus, if the "steady state" is stable, one could hypothetically ignore everything that happened in the prior system's "steady state".

At first look, we see that the system of (whether with constant or variable parameter

distributions) 150 is stable and not sensitive to initial conditions. The morphology (in our case the number of hair cells, sallets and rows of hair cells) of the lizard ear varies across families. We tested this hypothesis for different numbers of oscillators. By lowering the number of oscillators for fixed parameters and frequency ranges, the system starts showing sensitivity to initial conditions and becomes less stable. This behaviour is expected for a model that is nonlinear and complex enough to show chaotic behaviour. Thus, for a given set of parameters, there is a lower boundary for the number of oscillators enough for stable synchronization to occur.

Chapter 4

Hypothesis 2

Embedding roughness solely in the frequency distribution (i.e., modeling a unique tonotopic map) is sufficient to produce (stable) idiosyncratic spectra to a given simulated "ear".

As has been previously mentioned, each ear has its own set of peaks and valleys in SOAE spectra. At the same time, we know that each ear is also characterized by a unique tonotopic map (also referred to as a "fingerprint"). Thus, it is fair to hypothesize that variations in a spatial distribution of characteristic frequencies, across basilar papilla lead to the formation of idiosyncratic SOAE spectra. Meaning that a unique tonotopic map equals unique SOAE spectra. To test this hypothesis we are going to simulate a variety of frequency patterns. In this case, changes within the system parameters should be close to natural fluctuations. The easiest explanation that comes to mind is roughness in a characteristic frequency distribution. The term roughness itself is commonly used to determine irregularities in a frequency distribution. Thus, one way to present it is via a randomly generated noisy pattern of frequency fluctuations that are added to the initial frequency distribution. As by definition roughness could describe any sort of irregularities, another way to introduce it is via having by itself irregular frequency distribution which is a noisy "step-like" (when few neighbouring oscillators are at a similar characteristic frequency thus forming noisy plateaus in a frequency distribution). In such a way, we account for the fact, that hair cells in the ear are organized in rows of n hair cells (see Section 1.2.1). Especially as such a step-like distribution has been observed (Turner 1986). Overall, as we introduce roughness we can generate a new tonotopic map for each simulation and as a result, we expect to see unique spectra for each simulation with a new frequency distribution.

4.1 Results

In our simulations, we generate a rough tonotopic map by adding every time to the initial frequency distribution a new roughness pattern of a given amplitude (in percentage from the frequency of the first oscillator). We first generate a roughness pattern by randomly selecting values from -1 to 1 into an array of 150 data points and then correcting its amplitude to the corresponding value in [%]. Thus, we can obtain results for different roughness amplitudes with the same pattern and vice versa (different patterns with the same amplitude). Both is used to see what the differences within the spectra are caused by roughness and understang if frequency roughness could be source of unique ear and unique SOAE pattern.

As an example let us look at one of the representations of rough frequency distribution (one randomly selected pattern). Figure 4.1 shows the effect of frequency roughness on clustering, for a system of 150 oscillators with constant parameters (the same as for Figure 2.3, Vilfan and Duke (2008) model but 150 oscillators). The top left heatmap (subplot (a)) shows changes in simulated spectra for the same roughness pattern but different amplitude, thus we can study the effect of roughness amplitude on to the system (for a given roughness pattern). Up until 5% roughness, there are slight changes in spectra and after that, we see that the system starts to decluster. This leads to the formation of areas of narrow peaks superpositioning until clustering almost disappears. These results are based on one pattern and give an idea of how the amplitude of roughness affects clustering. As out of this we gain general estimations of what are roughness amplitudes that might be of interest to us (as a potential source of uniqueness of SOAE spectra), we need to see if expected results would be common for other roughness patterns. Thus, to see if we are able to generate unique spectral patterns, we do the opposite, each time we generate a new random pattern but with the same amplitude. Results for some of those simulations (2%, 5% and 6% roughness) are depicted by heatmaps in subplots (b) − (d). As we can see there are some slight shifts in peak locations and some shifts in peak height for both 2% and 5% roughnesses. Occasionally some declustering can be observed. However noticeable changes in clustering can be seen only for roughness not less than 6% (subplot (d)). But even those do not quite correspond to changes of different ears, as we are going to discuss later. Additionally, for some patterns (such as 1, 7 and 10 in the lower right subplot), we see desynchronization for lower frequencies. Figure 4.1 shows that the last peak in spectra is strongly defined and has the least fluctuations in its location. Furthermore, all three roughness amplitudes lead to relative peak broadening for some peaks.

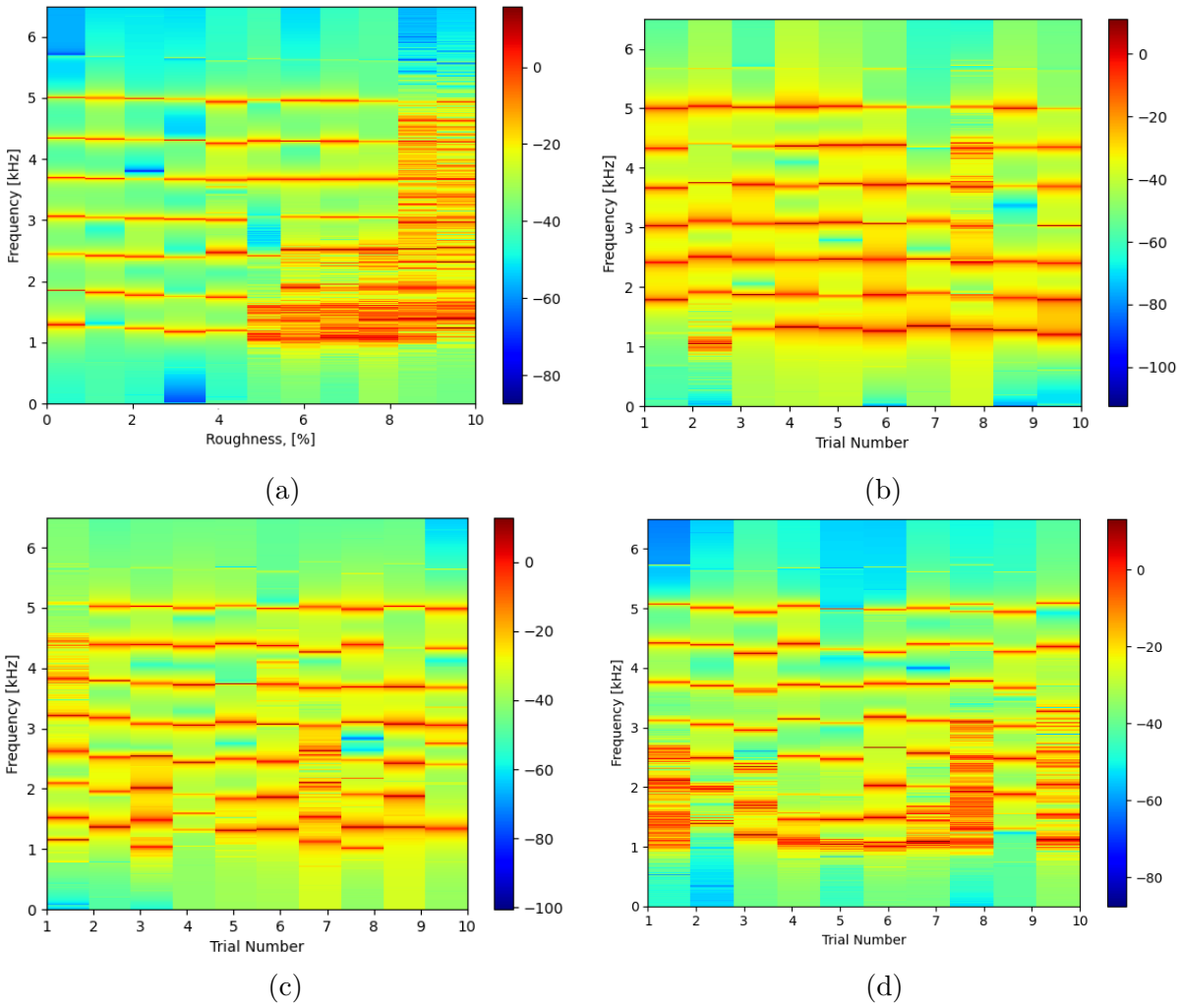

Figure 4.1: Effect of frequency roughness on clustering pattern. (a) results for different roughness amplitudes [%] with the same roughness pattern; (b) 10 different trials with roughness 2%; (c) 10 different trials with roughness 5%; (d) 10 different trials with roughness 6%

As we saw in Section 2.3.3, the resulting spectrum (as well as clustering pattern) for an anole-like model (mass and stiffness vary for each oscillator) the results differ from the one with constant parameters. Thus, let's see if, for the anole-like model, the differences in results with different roughness would be more distinguishable. And as the interest of our research is the anole inner ear, we are going to repeat the previous steps for the anole-like model. In the case of this model, we are using "primary parameters", but we are still having only a rough tonotopic map. To do so, we are using the approach from Section 2.3.3 to determine initial distributions of parameters, and adding roughness patterns for derived characteristic frequency distribution.

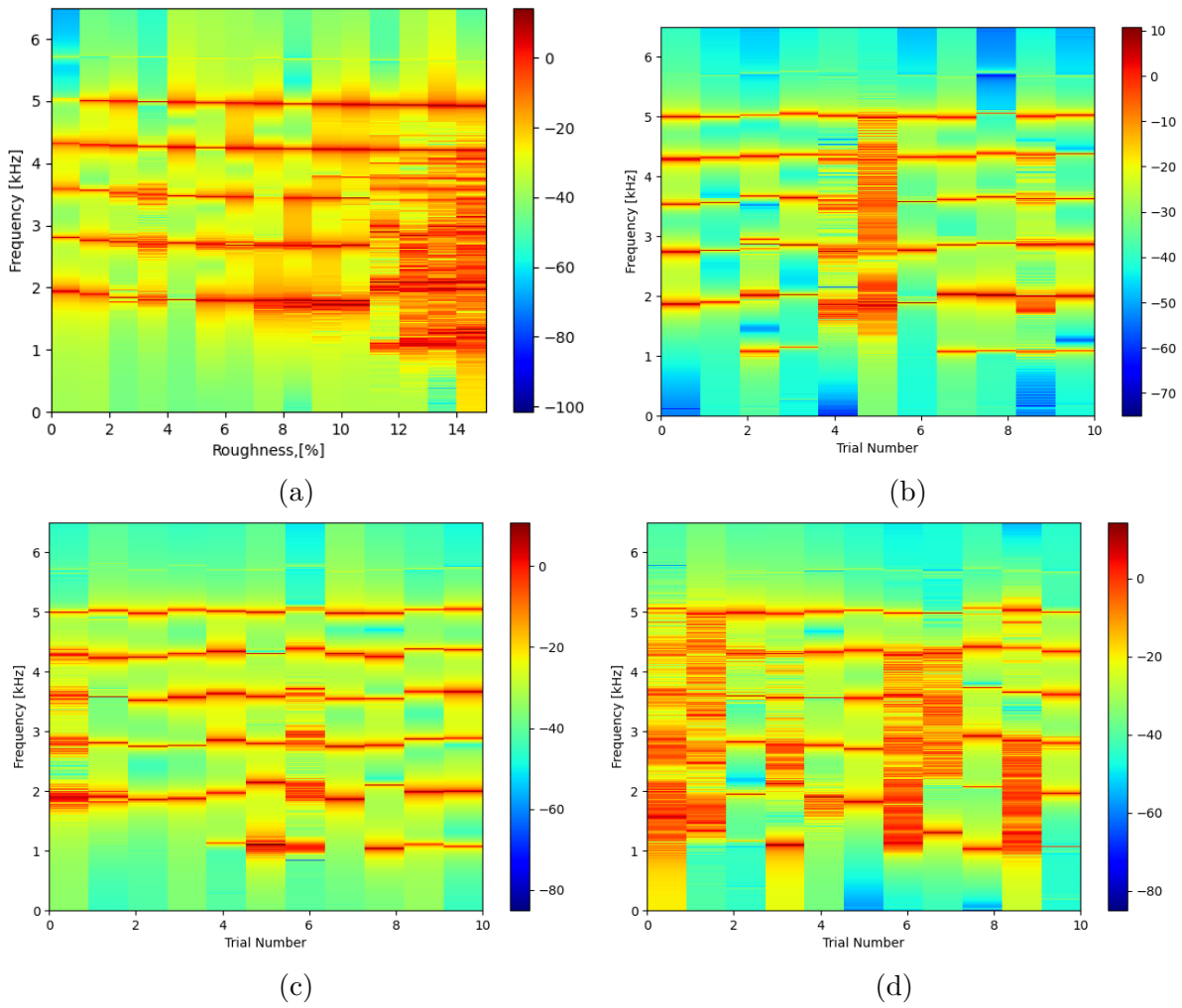

Figure 4.2: Effect of frequency roughness on clustering pattern for the anole-like model scenario (4). (a) results for different roughness amplitudes [%] with the same roughness pattern; (b) 10 different trials with roughness 2%; (c) 10 different trials with roughness 4%; (d) 10 different trials with roughness 7%

When roughness is added to characteristic frequency distribution in an anole-like model we also see that with an increase in roughness amplitude, the system starts to decluster, leading to peak widening and the presence of superposition. Figure 4.2 shows that a 7% roughness more often leads to a less synchronized system, which is consistent with what we saw previously. On the contrary, for 2% and 4% roughness, we start to see differences in the way the system synchronized for each pattern. Location of peaks between 1 and 3 kHz shifts with each simulation. But the higher frequency peaks stay within a small fluctuation region (the location of the peak is almost the same for each trial).

Now, let us look at the other way we can implement roughness, as we stated above it

can be done by dividing a tonotopic map into rows of n hair cells that are having similar or slightly different characteristic frequencies, thus making frequency distribution with approximately 38 noisy plateaus of 4 oscillators. As such a system is initially preclustered we would expect to see differences within sets of peaking frequencies in simulated spectra. But before testing this hypothesis, let us see if the system is not sensitive to initial conditions and maintains stability. As its behaviour might be similar to the one of 38 coupled oscillators. And as we suspected if we implement "step-like" frequency distribution in our model, it starts to be sensitive to the initial condition. Thus, if we are simulating such a system with random initial conditions and frequency roughness, we won't be able to determine whether new clustering patterns were formed mostly because of new roughness or initial conditions.

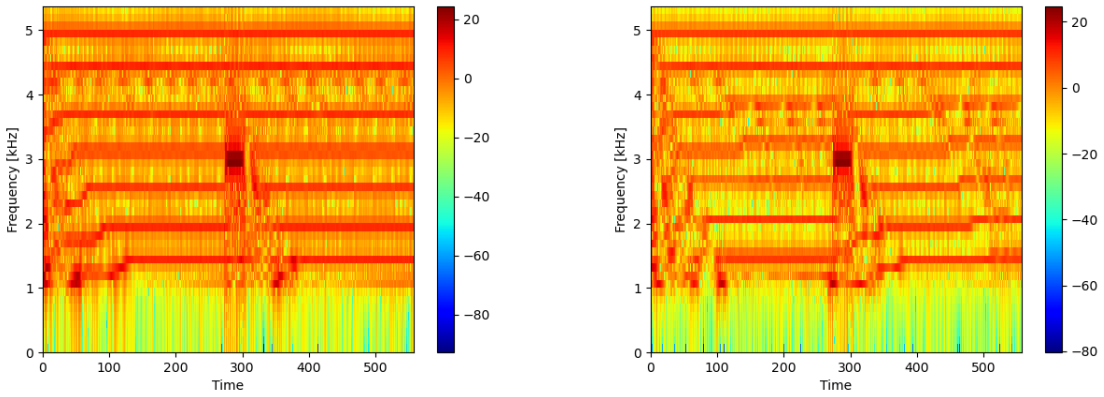

(a) (b)

Figure 4.3: Chain with "step-like" frequency distribution (rest of the parameters are constant), 38 steps, with a quick tone at 3 kHz present after the system reached a steady state. (a) Stable case; (b) Unstable case.

As we discussed in the previous chapter, we might ignore sensitivity to the initial condition if the model stays stable once it reaches a "steady state". Figures 4.3 and 4.4 show spectrograms for such systems with constant parameters and variable parameters respectively. As we can see both models depending on initial conditions could reach a stable "steady state" (subplots a) and an unstable "steady state" (subplots b). These results are in contrast to what we saw for a chain of 38 oscillators, as in that case system couldn't achieve a "steady state". These models were relatively stable, approximately 1/2 of the initial condition led to a quick peak return. As for the rest half of the results, we noticed that outcomes depicted by subplots (b) were relatively rare, the majority of unstable results were portrayed by a slight shift of peaks that stayed stable after

synchronization to the new pattern. It is important to state that our statements have been based only on observations from our simulations, and we didn't do any additional statistical analysis.

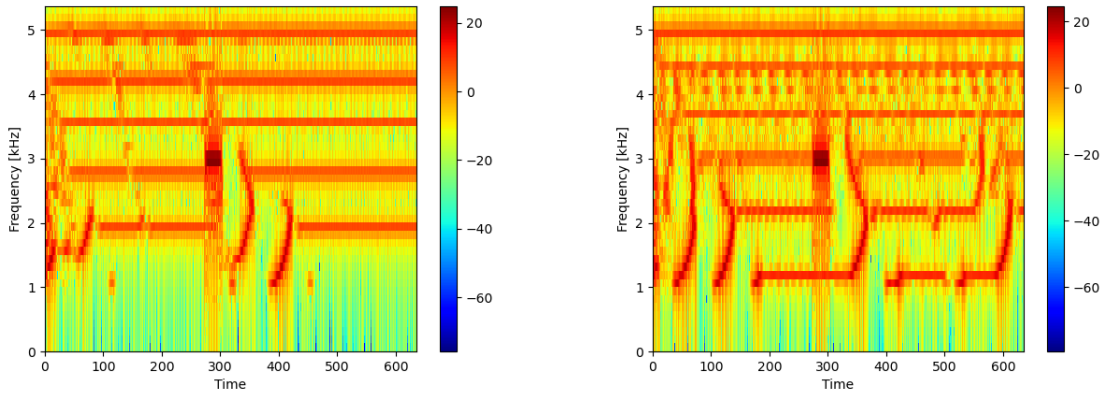

(a) (b)

Figure 4.4: Anole-like model with "exponential steps" frequency distribution, 38 steps, with a quick tone at 3 kHz present after the system reached a steady state. (a) stable case; (b) unstable case.

4.2 Discussion

As previously mentioned, in our simulated spectra we see slight variations in the peaky pattern by simulating morphological variations. However, for a model with constant parameters, those variations are within a small region such that they look like slight fluctuations up and down along the y-axis (frequency at which the peak is located) rather than each spectra having a unique pattern. At the same time, we are starting to see greater shifts for the anole-like model (for example 5% roughness, Figure 4.5 (a)), but the high-frequency peaks still shift only within a small region. At the first look we can see those inconsistencies by comparing 10 generated spectra for an anole-like model (scenario (4)) and 10 measured SOAE spectra (Figure 4.5). Even as we see shifts within cluster frequencies, we get resulting spectra that are similar to each other with minor shifts in peaking frequencies or the one with significant shifts only up to 4 kHz. Higher frequency peaks were present in all simulations and had less significant shifts (which is inconsistent with what we see in actual SOAE spectra). In measured SOAEs, we see strong changes not only in the locations of peaks but their height and width, which could be barely seen in simulated results. Thus, we can conclude that simply adding roughness to the exponential tonotopic map is not enough to simulate idiosyncratic SOAE-like spectra.

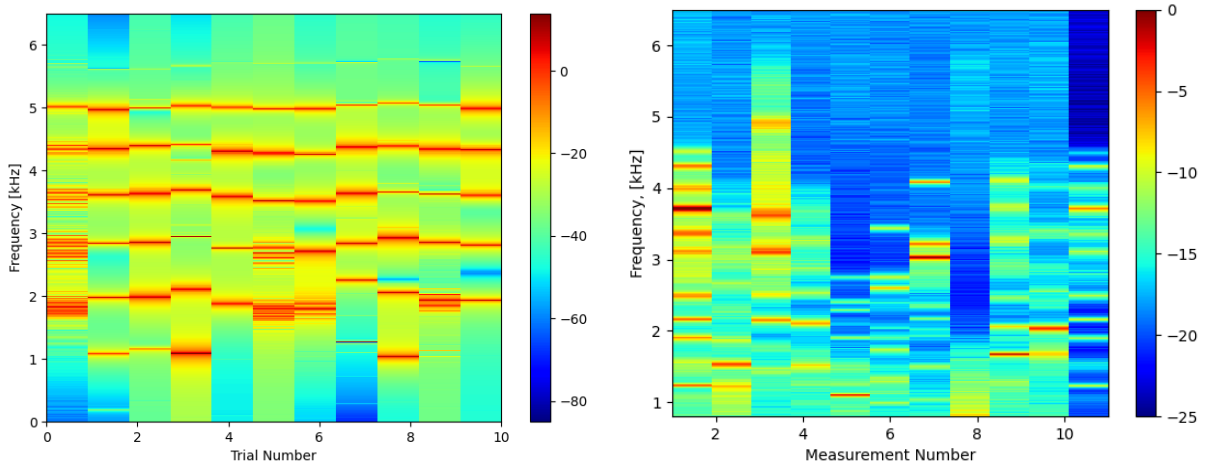

(a) Simulated (b) Measured

Figure 4.5: (a) Simulated spectra for different frequency roughness patterns of 5 % for anole-like model scenario (4), colorbar − magnitude [dB]. (b) Measured Anole SOAE spectra, each vertical line depicts spectra for a given measurement, colorbar − magnitude SPL [dB].

Adding roughness to a "step-like" exponential tonotopic map (assuming that the hair cells within a row are at almost the same characteristic frequency) leads to stronger differences (but yet not strong enough) between simulated spectral patterns. However, this system became sensitive to initial conditions. If we were to justify our estimation of possible reasons why the system could be sensitive to changes in initial conditions but stay stable as discussed in the previous chapter, this type of model would lead to additional sources of generating unique spectral patterns. But at the same time, that sort of change in clustering (peak) patterns is still inconsistent with the variety of patterns that measured SOAE spectra have. Thus, roughness embedded only in a frequency distribution is not sufficient to simulate unique SOAE-like spectra.

Chapter 5

Hypothesis 3

Embedding roughness in the distribution of hair bundle height (i.e., modeling morphological differences across individuals) is sufficient to produce (stable) idiosyncratic spectra to a given "ear.

As we concluded in the previous chapter, roughness added to the tonotopic map alone does not seem sufficient to explain idiosyncratic simulated SOAE spectra. Although the term roughness itself is commonly used to determine irregularities in a frequency distribution, another way to have a rough tonotopic map is by adding roughness to the hair cell bundle height distribution. Thus, in this research, the word "roughness" is not only limited to the noisiness of frequency distribution.

To state this hypothesis, we are using a passive consideration for the characteristic frequency of the oscillator and we assume that it only depends on the mass and stiffness of the oscillator (for a hair cell on the height of its bundle). In this case, roughness in height distribution would lead to roughness not only in the tonotopic map but in other resulting parameters (see Section 3.2.1). Similarly to the previous hypothesis, we suggest that variations in hair cell bundle height across basilar papilla lead to the formation of idiosyncratic SOAE spectra. This means that a unique tonotopic map in combination with unique distributions of coupling terms (d_I and d_R) equals unique SOAE spectra. To test this hypothesis we are going to simulate a variety of height roughness patterns added to the initial distribution. Thus, as we introduce roughness we can generate a new tonotopic map for each simulation and as a result, we expect to see unique spectra for each simulation with new height distribution.

5.1 Results

As the interest of our research is the anole inner ear, we are going to repeat the previous steps for the anole-like model. In the case of this model, we are using "primary parameters" and two of those parameters such as mass and stiffness (m_j and k_j) depend on height. And as we stated above roughness in height distribution would lead to roughness in the distribution of characteristic frequency. But before we start to study its effect, let us revise if we know how exactly our parameters depend on oscillator height (height of hair cell bundle). We need to understand that to determine the relationship between height and other parameters we are introducing many additional assumptions (for detailed explanation see Appendix A.1.1). Using the equations from Section 2.3 we can assume that $M_j \propto h_j$ and $K_j \propto 1/(h_j)^2$ meaning that $\omega_j \propto 1/(h_j)^{3/2}$. Based on this assumption to get an exponential tonotopic map the height distribution should be exponential as well, which is inconsistent with measurements done by Turner (1987). Due to the lack of information about hair cell bundle height and frequency distribution, we are using the assumption that $M_j \propto h_j$, $K_j \propto p_j/(h_j)^2$ and that height distribution is exponential, where p_j is a parameter that varies across chain to match exponential distributions of M_j, K_j, ω_j and h_j with their boundary values (see Appendix A.1.1). Thus, in this case, we first are generating an exponential height distribution, adding to it generated roughness pattern of a given amplitude [%] and after that deriving distributions of other parameters. The rest of the procedure is the same as in the previous chapter.

Figure 5.1 depicts an effect of height roughness on an anole-like model, left subplots correspond to scenario (2) and right subplots to scenario (3) that we used in the previous chapter (Section 2.3.3). In contrast to frequency roughness, for a given height roughness pattern (subplots (a) and (b)) height frequency clusters start desynchronizing leading to the disappearance of a strongly defined peak around 5 kHz. And again we need to account that to subplots represent results for one specific roughness pattern and thus we use it to have a general understanding of the potential outcome of such roughness strength. And if we generate several spectra with a given amplitude (subplots in the lower panel Figure 5.1) we see that this model has the same limitation as a model with constant parameters not being able to have a significant shift in higher frequency peaks. Overall, most roughnesses led to results with strong variety, which is an improvement from what the model with constant parameters gave, and at the same time almost identical to results of the "anole-like" model with frequency roughness.

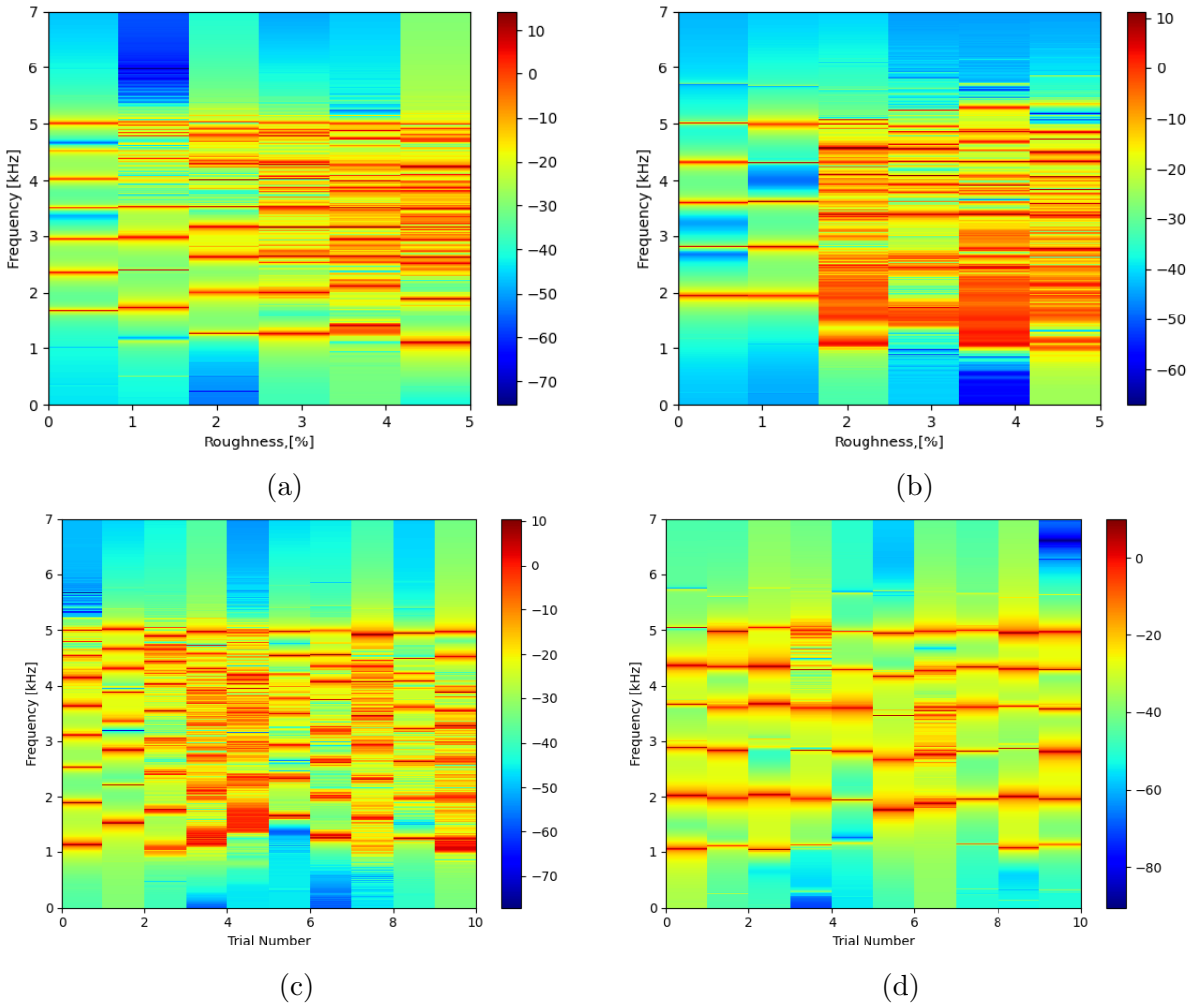

Figure 5.1: Effect of height roughness on clustering pattern for anole-like models. Top panels Results for different roughness amplitudes [%] with the same roughness pattern: (a) scenario (3) ; (b) scenario (4); Lower panels, 10 different trials with roughness 1%: (c) scenario (3); (d) scenario (4)

5.2 Discussion

As roughness in height would lead to roughness in mass and stiffness it would lead to roughness in frequency and at least coupling parameters (d_{Ij}, d_{Rj}) distributions, thus we would assume stronger effect than in case of just frequency roughness. As we saw in previous sections, even roughness of amplitude as small as $< 2\%$ could change the spectral pattern. Figure 5.2 depicts results that are similar to the previous hypothesis, but in this case, for a some combination of roughness amplitude and coupling (k, γ) we can see strong differences. One of the key limitations similar to results from the previous hypothesis is

still a sharp peak around 5 kHz. That peak is not only sharp and strongly defined, but even with stronger roughness it still manages to stay within a small fluctuation from 5 kHz. Another factor is that for measured SOAEs we see that areas with no peas or with low peaks are not limited only to the lower frequencies. Although in this scenario, we are able to generate unique spectral patterns but are still inconsistent with "unique ears". Consequently, it becomes clear that morphological differences on itself does not lead to the generation of a unique ear, there are some physiological changes happening to determine a unique ear and as a result idiosyncratic SOAE spectra. Those changes might be embedded in active term and a nonlinear term, as has been studied previously (Wit et al., 2020; Gelfand et al., 2010).

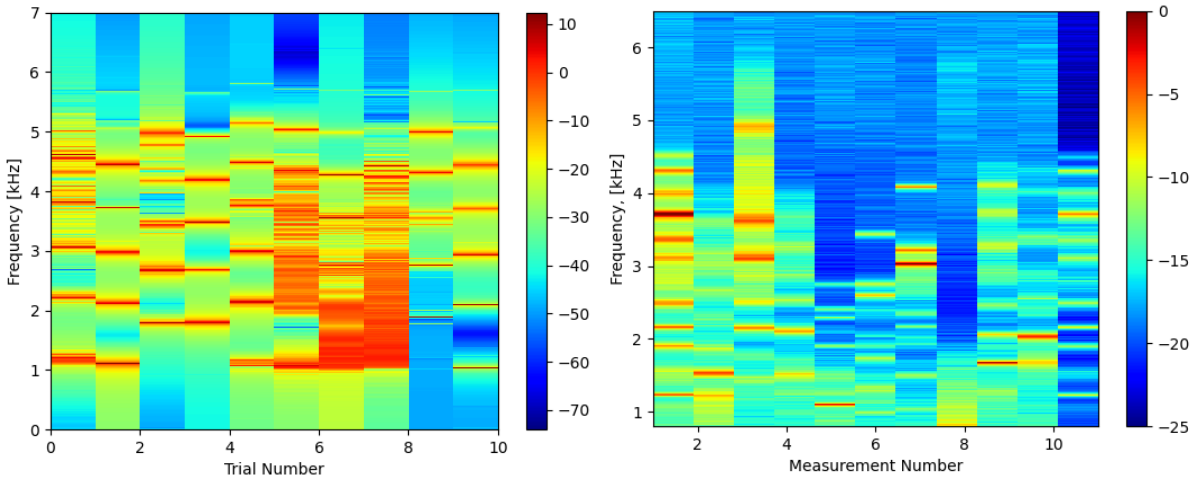

(a) Simulated (b) Measured

Figure 5.2: (a) Simulated spectra for different height roughness patterns of 1.5 % for anole-like model scenario (4), colorbar − magnitude [dB]. (b) Measured Anole SOAE spectra, each vertical line depicts spectra for a given measurement, colorbar − magnitude SPL [dB] (Same as Figure 4.5(b)).

Chapter 6

Hypothesis 4

Broader peaks can be simulated by the inclusion of noise (either local or external/global), which causes interactions between clusters leading to frequency modulations (FMs).

Each peak in a lizard SOAE spectra has its own unique characteristics such as the peak width. The peaks in measured SOAEs are much wider than the ones shown in previous simulations. Thus, we suggest that one of the possible sources of spectral peak broadening is noise, whether of thermal or acoustic origin, as in actual ear hair cells are subject to noise. By saying that noise is a possible source of peak broadening we mean that it leads to fluctuations in cluster frequencies. Within such a complex living system, there are many sources of randomness (we even based our previous hypotheses on two of them). This means that noise is such a broad term, so to narrow it down, we are using additive noise in the form of an external term added to the equation of motion (Section 2.4). Even in this case, there can be many sources of noise, we introduce two terms: external noise (also can be referred to as global, for example, the noise of stapes) and oscillator noise (also can be referred to as local, for example, the noise of a hair cell). To test this hypothesis we are going to introduce noise of varying amplitudes into the system and look into the results for each simulation after performing spectral averaging. Thus, by studying different levels of noise, we can analyze its impact on the spectral characteristics of the simulated peaks. Additive noise has already been introduced to the models of SOAE generation (Vilfan and Duke, 2008; Wit et al.,2020; etc.) and it led to wider simulated peaks. But those studies were lacking on rationales and explanations for why peaks are broadening. One possible explanation can be that noise, either intrinsic (e.g., thermal agitation) or external, can cause perturbations and affect synchronization characteristics (leading to synchronization/cluster frequency fluctuations).

6.1 Results

As mentioned above, to test this hypothesis we focus specifically on additive noise, such as oscillator noise, which has a unique value for each oscillator $\xi_j(t)$ and external noise $\xi(t)$, which is the same for all oscillators. Below we present how those two types of noises affect the way oscillators synchronize. So we generate a noise array by randomly grabbing a new value from a normal and by changing its standard deviation we control its amplitude. Then for each simulation, a noisy array of a given amplitude is generated and transformed into a function which is added to the system (see Section 2.4). To visualize the effect of the noise we use a heatmap where each vertical line is an averaged spectrum (40 spectral averages) for a given noise level (represented by standard deviation, sigma from 0 to $700 * 10^{-3}$) and colorbar is showing magnitude in [dB].

6.1.1 External Noise

First, we are focusing on external noise (also referred to as global), because it is a type of noise that is the same for all oscillators. As external noise is a broader term, it allows us to have the freedom of choice on what color of noise to choose. Therefore, we are using white noise without and with a lowpass filter (at 14.3 kHz). The last one has been used for both time-saving purposes and to mimic a brown noise.

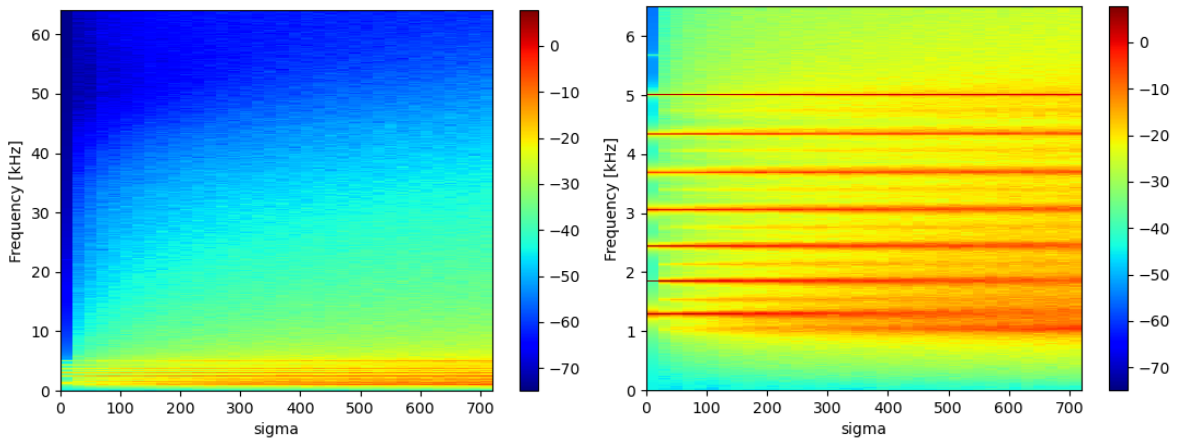

(a) (b)

Figure 6.1: (a) Heat map that represents changes in spectra with an increase in external noise (standard deviation sigma from 0 to $700 * 10^{-3}$) and (b) zoomed-in version. Colorbar corresponds to the magnitude of spectra in dB.

Figures 6.1 and 6.2 show spectral changes with the inclusion of white noise and filtered white noise respectively, for the system of 150 oscillators with constant parameters (all

parameters are as used before). The subplots (b) are zoomed-in versions of the subplots (a) providing a closer look into changes within a region from 0 to 7 kHz. As was expected both noises led to peak broadening. As the amplitude of the noise increased, the noise floor started to increase. At the same time by increasing the noise we slowly start to broaden peaks more. Peak blurring starts at lower frequencies (as expected by the nature of low pass filter, for filtered noise this process was more dramatic). In the case of the brown (filtered) noise peaks broadens up until they fade into the noise floor. As in the case of frequency roughness, the peak of the last cluster (last peak) is strongly defined for both filtered and white noise.

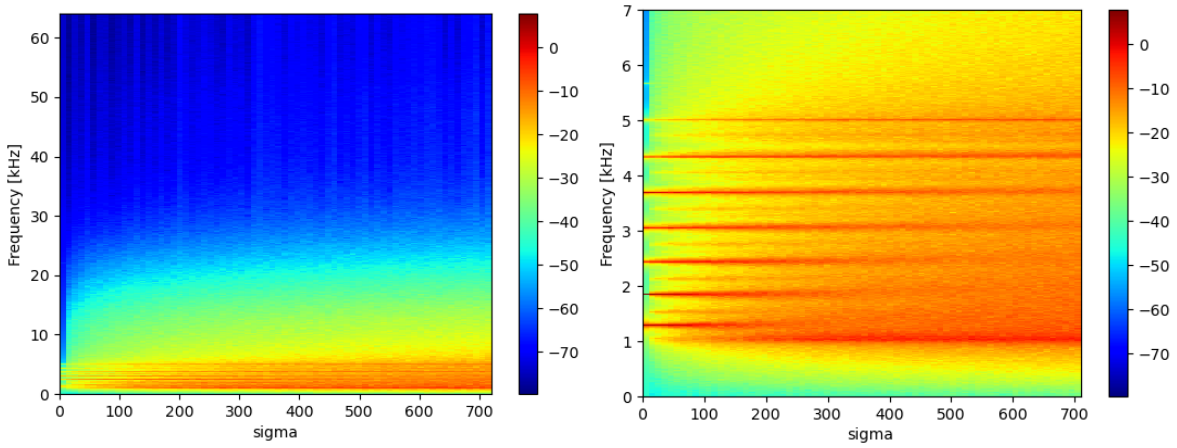

(a) (b)

Figure 6.2: (a) Heat map that represents changes in spectra with an increase in filtered external noise (standard deviation sigma from 0 to $700 * 10^{-3}$) and (b) zoomed-in version. Colorbar corresponds to the magnitude of spectra in dB.

Similarly to peak broadening, right away for both colors of noises, we can notice intermediate peaks in between our "7 main peaks" from the first column in presented heatmaps (or from Figure 2.3). Although, those peaks are lower in magnitude than dominant peaks (peaks that denote a dominant frequency in clustering) but still have their characteristic width and height. Thus, for our analysis, we would still consider them peaks even if for higher noise levels they blur and somewhat merge into the noise. The appearance of intermediate peaks is presumably a "second layer of synchronization".

It is also worth mentioning that even filtered noise didn't save that much time. Thus, there is no need in our case to use filtered noise if it was needed only for time-saving purposes. For the anole-like model, we are using just external noise. As we can see in Figure 6.3 with the introduction of noise similar to the previous model, peaks started to broaden and we see the second layer of synchronization. At the same time because this scenario originally has fewer clusters (indicating frequencies of 5 main peaks) with more

oscillators in the first clusters, we now see that the first cluster causes the appearance of two peaks by the second layer of synchronization. And these two peaks are the first to blur with the increase in noise. Other peaks have just one new peak in between them.

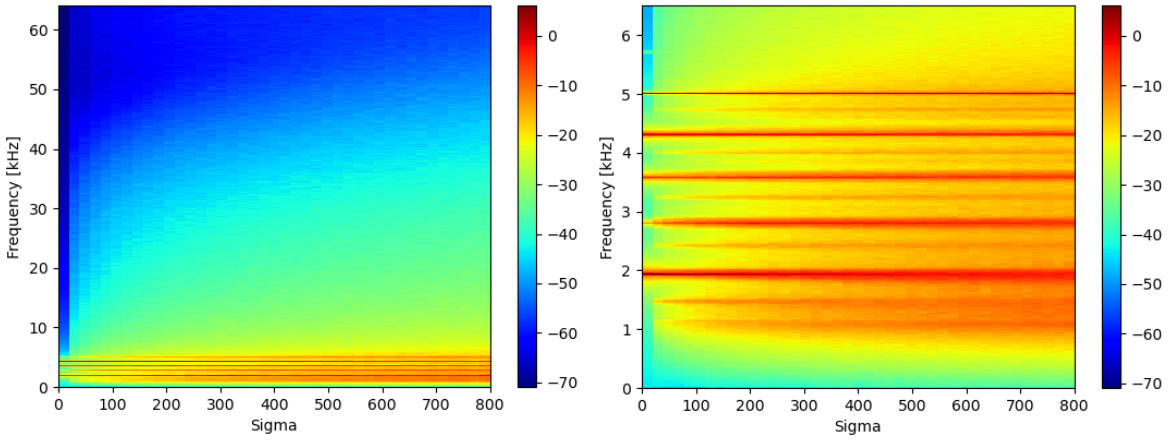

(a) (b)

Figure 6.3: Anole-like model (scenario 4) with external noise. (a) Heat map that represents changes in spectra with an increase in external noise (standard deviation sigma from 0 to $800 * 10^{-3}$) and (b) zoomed-in version. Colorbar corresponds to the magnitude of spectra in dB.

6.1.2 Oscillator Noise

As the source of oscillator noise (also referred to as local) clearly is thermal noise due to Brownian motion, it can be generated as white noise. By its nature, this noise is unique to a given oscillator. Similarly to external noise, we plot the results for both models with constant parameters and an anole-like model with the introduction of oscillator noise using heatmaps.

From figure 6.4 we see that hair cell noise also leads to peak broadening and the appearance of intermediate peaks. In contrast to external noise, peaks stay wider and clearly defined pass $\sigma > 900 * 10^{-3}$. We still see that the broadening of the first few peaks is stronger than the one at a higher frequency, but at the same time, it is not as dramatic as for external noise. Another unique feature of this case is that the noise floor increases smoothly across the oscillatory region and is minimized outside that region, such that the outside oscillatory region noise floor is similar to what we expect for temporal averaging. We can notice that comparing zoomed-in (subplot on the right) and zoom-out (left subplot) heatmaps, on the zoomed-out scale, the noise floor looks somewhat similar to filtered noise (noise floor dramatically decreases past specific frequency) but with much better SNR and defined peaks.

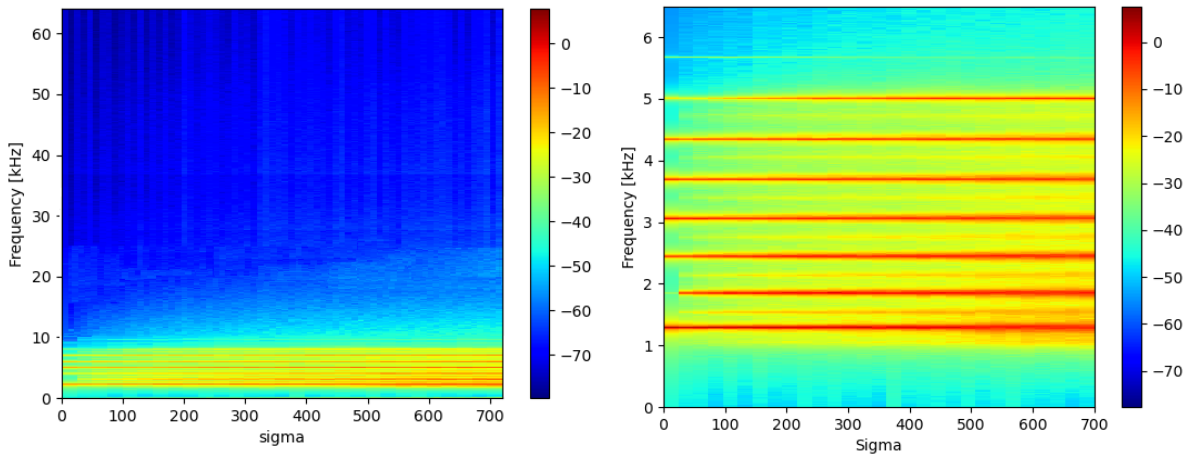

(a) (b)

Figure 6.4: (a) Heat map that represents changes in spectra with an increase in oscillator noise (standard deviation sigma from 0 to $700 * 10^{-3}$) and (b) zoomed-in version. Colorbar corresponds to the magnitude of spectra in dB.

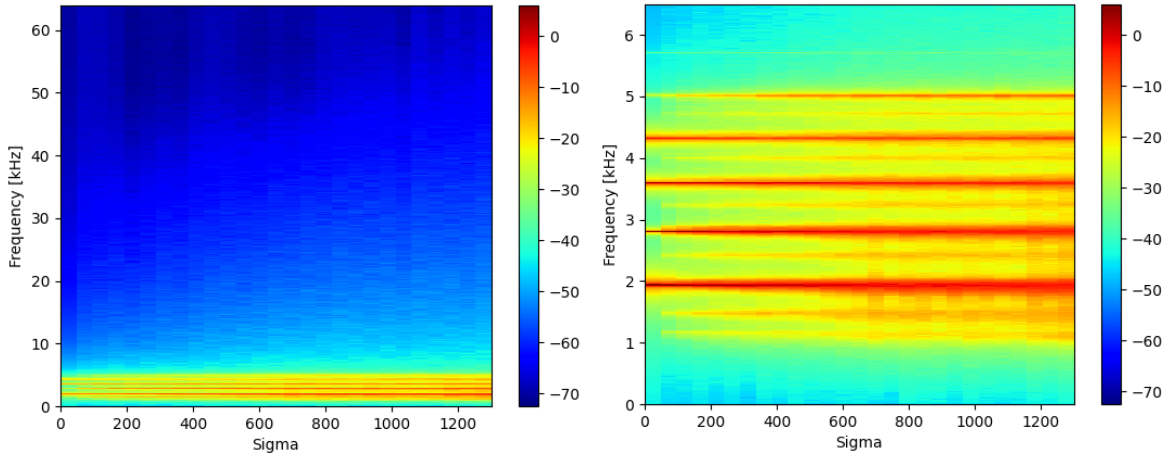

(a) (b)

Figure 6.5: Anole-like model (scenario 4) with local noise. (a) Heat map that represents changes in spectra with an increase in oscillator noise (standard deviation sigma from 0 to $1300 * 10^{-3}$) and (b) zoomed-in version. Colorbar corresponds to the magnitude of spectra in dB.

Figure 6.5 shows that oscillator noise has a similar "anole-like" model effect to the one it has on the model with constant parameter distribution. As σ increases from 0 to $1300 * 10^{-3}$, we see that peaks slowly broaden and start to blur. As we stated when describing the effect of external noise on the "anole-like" model, as we have 5 primary clusters and 1st cluster contains more oscillators with the introduction of noise we have two peaks induced by the second layer of synchronization before the first primary

peak. Overall, for an anole-like model the tendency of peak broadening, a second layer of synchronization, and a lower noise floor outside the oscillatory region stay the same.

6.2 Discussion

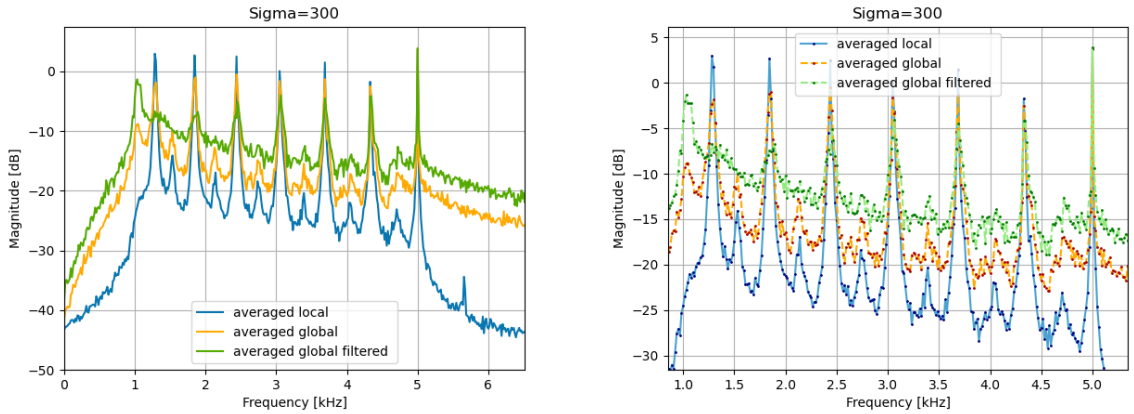

(a) (b)

Figure 6.6: Effect of 3 different noises types, noise amplitude is the same amplitude, in subplot (b) darker circles represent actual data point.

To compare and discuss the effect of noise on the system, let us look at spectra from three types of noises (external, external with a lowpass filter and local) with the same $\sigma = 300 * 10^{-3}$ (Figure 6.6). Here we clearly can see how peaks blur in case of external noise. When spectra are moved to the same scale, we can see that for both external noises peaks in between "main peaks" moved to noise floor level or that the first main peak for filtered noise was entrained by it. Subfigure (b) shows peak broadening, we can see that now we have more points at the top of the peak. All of the noises led to peaks being still relatively pointy but sharp (the noiseless system has one data point at the top of each peak). But at the same time, we still have this strongly defined sharp peak at $5kHz$, a result like this is not consistent with SOAE spectra. Figure 6.6 shows a difference between noise floor levels for each case. As has been mentioned, local noise has a rise in noise floor level only within the oscillatory region, such that it is similar to the outcome of temporal averaging. We suggest that this occurs because of the nature of how we obtain simulated SOAE-like waveforms, as we sum waveforms from each oscillator. In this case the process of summation for oscillation at frequencies that are outside the oscillatory region (typically between 1 to 5 kHz) acts similar to temporal averaging as those oscillations are noise that is different for each oscillator.

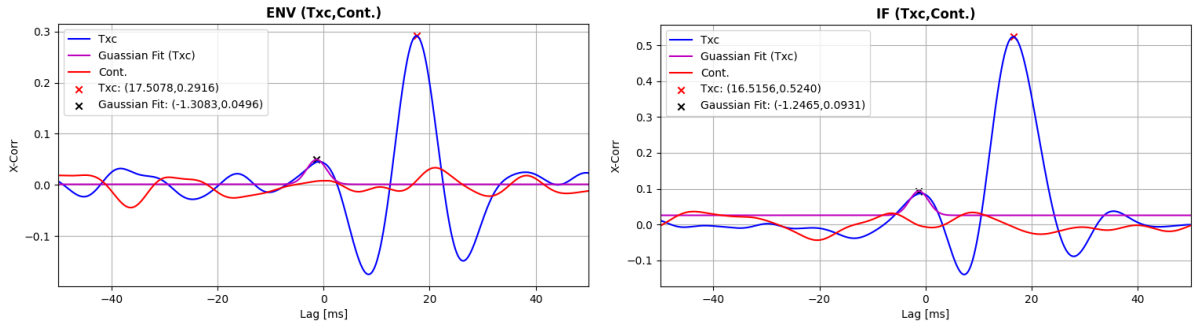

(a) (b)

Figure 6.7: Correlation analysis for "main peak" 3 and 4, $\sigma = 0.1$, roughness − no roughness, noise − local noise; (a) amplitude modulation (AM); (b) frequency modulation (FM).

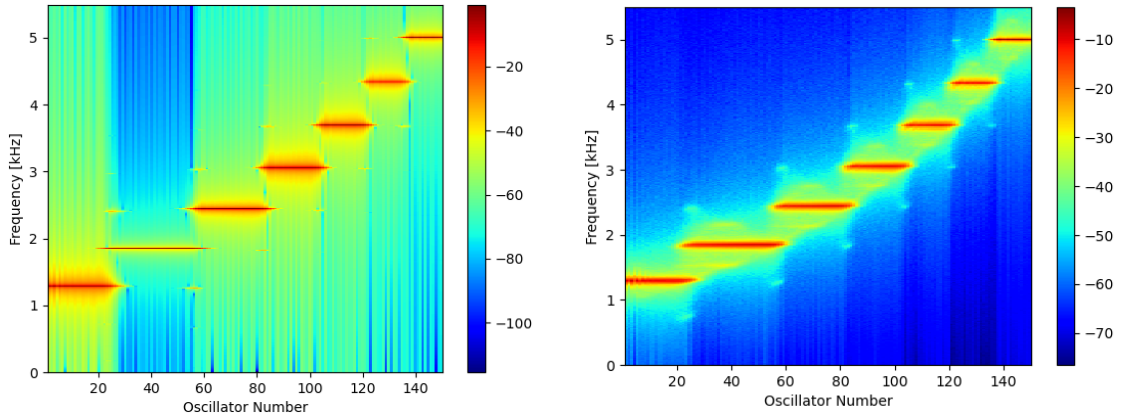

(a) (b)

Figure 6.8: Clustering heatmap; (a) noiseless (same as Figure 2.2 (c)); (b) with local noise $\sigma = 300 * 10^{-3}$.

To better understand the nature of peak broadening in our research we used correlation analysis. We conduct correlation analysis for filtered individual peaks from simulated spectra (see Appendix A.1.2). Overall, as we noticed for both local and external noise, neighbouring "main peaks" (tall peaks) have both AM and FM correlation with a maximum value approximately between $0.09 - 0.6$ (as an example see Figure **??**). We also notice that, "secondary peaks" (shorter peaks in between tall peaks) are not correlated with each other but are FM correlated with neighbouring "main peaks". We observed occasional weak FM correlations even for the peaks that are 2nd nearest neighbours (for example 2 and 4). At the same time, for the noiseless system we don't have a distinct correlation between peaks (noiseless spectra only have main peaks). This possibly can be

explained by assuming that with the introduction of noise the interaction between oscillators from different neighbouring clusters causes frequency modulations. We can see that in Figure 6.8 clusters became thicker with the introduction of the noise and a second layer of synchronization has been formed. One of the possible reasons why "secondary" peaks are not correlated with each other is that there is minimum overlap between oscillators that are involved in the second layer of synchronization. In contrast, we see significant overlap for "main clusters" for both noisy and noiseless systems, which leads us to the open question: why are peaks in noiseless system not correlated.

As expected both types of noise led to peak broadening and peak width increased with an increase in noise amplitude. At the same time, the inclusion of both types of noise resulted in the "second layer of synchronization" in the form of formed peaks in between initial peaks. For the local noise, the observed noise floor was lower than for the external and the increase of noise floor was within the oscillatory region (which is consistent with the way local and external noise are determined).

Chapter 7

Overall Discussion

As a focus of our research, we use an established model (Vilfa and Duke, 2008) that depicts an inner ear as a chain for coupled limit-cycle oscillators. It has been already observed that this type of model gives a possible explanation of how SOAE spectral peaks are generated, stating that the critical component is not individual by collective dynamics. Hair cells synchronize within a cluster (group of oscillators whose dominant frequency is the same) and the number of clusters and their frequency would correspond to number and frequencies of peaks in generated spectra. As we modify the model to correspond inner ear with free-standing hair cells, the outcome would still support that theory, introducing a slightly different synchronization pattern. This means that these types of models are potentially capable of simulating the ears of different vertebrates. At the same time, while modeling ears with fewer oscillators but the same range of characteristic frequencies (anole ear with the assumption that each row of hair cells is represented by 1 oscillator) failed to stay insensitive to initial conditions and also became unstable. It is fair to state that we came to that conclusion based only on results from our simulations (we do not dive into the mathematical relationship between parameters and the number of oscillators for the system to stay stable and maintain a clustering pattern). Some of the limitations that we have faced were related to us lacking the knowledge of what values some of the parameters should have that correspond to the actual system. As we stated in Chapter 3 the system that represents an inner ear should be stable and insensitive to initial conditions. The results raise a point for discussion, whether we can ignore the sensitivity of the system to the initial condition if it is stable. One might say that sensitivity to initial conditions is irrelevant in our case as the actual ear doesn't have a time when there is no oscillations or any other perturbations, such that the initial time is then system returned back to its steady state after discontinuing external perturbations (achieving conditions acceptable to measure SOAEs). At the same time, we noticed that for simulations as we change

initial conditions, the time it takes for the system to return to its "steady-state" changes. This could be checked for different types of lizards and different individuals, looking if the time it takes for spectra to return after discontinuing external tone is identical for the same individual during different measurements, for different individuals within one type of lizard and different types of lizards (possible type of lizards: green Anole, Gecko and Bobtail lizard). Talking about different individuals, we already mentioned that each ear has a unique morphology and a unique SOAE spectral pattern. In our research, we checked the hypothesis that idiosyncratic spectra are a direct result of unique morphology. As we concluded that morphological changes within the ear (such as hair cell frequency of bundle height) lead to slight peak shifts and in some cases can cause lower frequency peaks to disappear, but in general it doesn't cause any major change to the spectra, thus not enough to generate unique SOAE spectra. We suggest that physiological differences between ears together with morphological differences can lead to the unique set of peaks and valleys in SOAE spectra. As has been suggested (Gelfand et al., 2010; Wit et al., 2020) physiological changes could be modeled by adding specific roughness to active and nonlinear term distributions. Another point for the discussion is the way we implement characteristic frequency, in our model we use passive representation, it depends only on morphology, but the fact that characteristic frequency changes with changes in temperature might suggest that we might include the dependence of characteristic frequency on physiology. This is a possible way in which this model could be extended, but one needs to be careful that this not only makes sense from a mathematical but also from a physical point of view.

As was hypothesized, the introduction of noise to the model resulted in the broadening of peaks, with their width expanding as the noise amplitude increased. Simultaneously, noise introduced a "second layer of synchronization," characterized by the emergence of additional peaks situated between the "main peaks". We suggest that in noisy spectra peaks are broader because noise causes interactions between clusters leading to FMs. We observed weak FM correlations between second neighbouring "main peaks" (for example peak 3 and 5), both AM and FM correlations between neighbouring "main peaks" and weak FM correlations between "main peak" and neighbouring short peaks (from the second layer of synchronization). Although this analysis shed some light on cellular cooperativity, there still are many yet unanswered questions (for example, why AM correlations are less occurring than FM correlations as in the case of SOAE spectra it is the opposite). Thus, we would further look into the correlation analysis of simulated spectra, with the intention of potentially wrapping the obtained results with those presented in this thesis into both a paper and a conference poster.

This model gave insightful information about possible interactions between hair cells and still might be useful for some research based on the type of questions they are asking. However, this model still has a lot of assumptions that might be a source of it's limitations. One of those assumptions is to ignore the 2D organization of hair cells along the basilar papilla. For modeling an anole case this assumption gives us an uncertainty on how exactly to model in 1D. This could be simply fixed by a 2D formulation of nearest-neighbour coupling. At the same time it raises a new set of questions. How are the oscillators in the same row coupled? Do we account for 2D motion? In its simplest form, the hair cell is coupled to multiple nearest neighbours (2-4 depending on its location) and oscillators within a row (y-axis) are coupled in such a way that the x-axis projection of coupling is the same as coupling between oscillators in neighbouring rows. The limited number of simulations we did led to the system being unsynchronised and not reaching its "steady-state" The logical way to evolve from nearest-neighbour coupling is to shift towards nearest-neighbour and global (via basilar papilla) coupling as suggested previously in Section 2.1.3.2 especially for ears with free-standing hair cells. This model would help to look into the system from two scales, as hair cells could be affected by external tones via basilar papilla and directly by local noise. At the same time, such a shift would help us to extend it into a system of two coupled ears. The model that represents a system of two coupled ears can give us insight into correlations between them and possibly explain some results that are yet unclear. All these modifications still do not change the fact that this model is built around the assumption that hair cells behave as limit-cycle oscillators and can oscillate spontaneously, as this assumption has not yet been experimentally proven or disproven. A forward-looking point is whether the SOAE generation process could be explained by a system of coupled noise-driven active but not limit-cycle oscillators. A limited number of simulations didn't lead to synchronized oscillation, as it is mostly due to our lack of knowledge on what parameters to choose. To further proceed with this system one needs to mathematically analyze under what conditions such a model could have oscillatory behaviour and reach a "steady state".

Overall, by definition this is a simplified representation of the actual system or process. In our case, the main question is what is the simplest model that can explain how the ear works while describing the inner ear dynamics. This model is complex enough, such that we can turn various knobs to make its outcome mimic SOAE spectra, but this is not our goal. Our goal is actually to understand what is going on inside the ear, and which process leads to SOAE generation. Through that lens the benchmark is that the model should be falsifiable. Thus, even though the model is based on an assumption that has not been experimentally proven, it has been useful in providing information on how the ear

works and predicting the outcomes. However, based on everything we have discovered in our research, I would like to conclude that in order to gain new information and test new predictions, we need to move toward another type of model. At the same time, the idea of describing SOAE generation as a by-product of the collective should not be abandoned, as it still has potential.

Bibliography

[1] Bergevin, C. (2016). Introducing global coupling to nearest-neighbour models of SOAE generation. Poster presented at 39th ARO MidWinter Meeting, San Diego, CA

[2] Bergevin, C., & Shera, C. A. (2010). Coherent reflection without travelling waves: on the origin of long-latency otoacoustic emissions in lizards. The Journal of the Acoustical Society of America, 127(4), 2398–2409. https://doi.org/10.1121/1.3303977

[3] Bergevin, C., Salerno, A. (2015). Dynamics of spontaneous otoacoustic emissions. AIP Conference Proceedings 31 December 2015; 1703 (1): 090024. https://doi.org/10.1063/1.4939422

[4] Bialek, W. (2012). Biophysics: Searching for Principles. Princeton University Press.

[5] Fettiplace, R. (2020). Diverse Mechanisms of Sound Frequency Discrimination in the Vertebrate Cochlea. Trends in Neurosciences, 43, 88-102.

[6] Fruth, F., Jülicher, F., Lindner, B. (2014). An active oscillator model describes the statistics of spontaneous otoacoustic emissions. Biophys. J. 107, 815e824.

[7] Freeman, D. M., & Weiss, T. F. (1988). The role of fluid inertia in mechanical stimulation of hair cells. Hearing research, 35(2-3), 201–207. https://doi.org/10.1016/0378-5955(88)90118-9

[8] Gelfand M, Piro O, Magnasco MO, Hudspeth AJ (2010) Interactions between Hair Cells Shape Spontaneous Otoacoustic Emissions in a Model of the Tokay Gecko's Cochlea. PLoS ONE 5(6): e11116. doi:10.1371/journal.pone.0011116

[9] Gold T (1948). Hearing. II. The physical basis of the action of the cochlea. Proc Roy Soc Lond B 135: 492-498.

[10] Hudspeth, AJ (2008). Making an effort to listen: mechanical amplification in the ear. Neuron 59(4): 530-45.

[11] Köppl, C., & Manley, G. A. (1993). Spontaneous otoacoustic emissions in the bobtail lizard. I: General characteristics. Hearing research, 71(1-2), 157–169. https://doi.org/10.1016/0378-5955(93)90031-u

[12] Manley GA, Köppl C. What have lizard ears taught us about auditory physiology? Hear Res. 2008 Apr;238(1-2):3-11. doi: 10.1016/j.heares.2007.09.011. Epub 2007 Oct 6. PMID: 17983712.

[13] Martin, P., Hudspeth, A. J., & Jülicher, F. (2001). Comparison of a hair bundle's spontaneous oscillations with its response to mechanical stimulation reveals the underlying active process. Proceedings of the National Academy of Sciences of the United States of America, 98(25), 14380–14385. https://doi.org/10.1073/pnas.251530598

[14] Miller M. R. (1981). Scanning electron microscope studies of the auditory papillae of some iguanid lizards. The American journal of anatomy, 162(1), 55–72. https://doi.org/10.1002/aja.1001620106

[15] Negandhi, J., Bergevin, C., Harrison, R. V. (2018). Scanning Electron Microscopy of the Basilar Papilla of the Lizard (Anolis Carolinensis). Canadian Acoustics, 46(1), 7–12. https://jcaa.caa-aca.ca/index.php/jcaa/article/view/3058

[16] Shera C. A. (2015). The spiral staircase: tonotopic microstructure and cochlear tuning. The Journal of neuroscience : the official journal of the Society for Neuroscience, 35(11), 4683–4690. https://doi.org/10.1523/JNEUROSCI.4788-14.2015

[17] Turner R. G. (1987). Neural tuning in the granite spiny lizard. Hearing research, 26(3), 287–299. https://doi.org/10.1016/0378-5955(87)90064-5

[18] Vilfan, A., & Duke, T. (2008). Frequency clustering in spontaneous otoacoustic emissions from a lizard's ear. Biophysical journal, 95(10), 4622–4630. https://doi.org/10.1529/biophysj.108.130286

[19] Wit, H. P., Manley, G. A., & van Dijk, P. (2020). Modeling the characteristics of spontaneous otoacoustic emissions in lizards. Hearing Research, 385, [107840]. https://doi.org/10.1016/j.heares.2019.107840

Appendix A

A.1 Supplementary information

A.1.1 Relationship between height and frequency distribution

In this section, we are going to look into a possible relationship between hair cell bundle height and other parameters. We need to understand that to determine that we are introducing many additional assumptions. To determine the mass of the hair cell we have equation $M_j = \rho h_j \pi \frac{d}{2}^2$, where d is the diameter of the bundle (approximately the same for all hair cell bundles $d = 10\mu m$), making this our first assumption. Hair bundle stiffness can be written $K_j = N_{Sj} \frac{1}{h_j{}^2} * K_{sr}$ where N_{Sj} is the number of stereocilia, K_{sr} is the rotational stiffness of single stereocilia, we can assume that N_{Sj} is constant to some order and equals approximately 50. Using these equations we can assume that $M_j \propto h_j$ and $K_j \propto 1/(h_j)^2$ meaning that $\omega_j \propto 1/(h_j)^{3/2}$. At the same time we have $\frac{K_{150}}{K_1} = 8.33$ and $\frac{h_1}{h_{150}} = 9$, $(\frac{\omega_{150}}{\omega_1})^2 = 25$ and $\frac{h_1}{h_{150}} = 27$ this suggests that N_{Sj} has a slight variation, which would be of use later in this chapter.

We know that the tonotopic map is exponential thus based on this assumption to get an exponential tonotopic map the height distribution should be exponential as well, which is inconsistent with measurements done by Turner (1987) as we can see in Figure A.1 and Figure A.2. Measured frequency distribution could have some curvature to it (has been observed in other species) but the times it is observed curve faces opposite way. This observation and the fact that only for exponential distribution, we have a fully synchronized system (Figure A.3) lead to the conclusion that we need to use exponential height distribution.

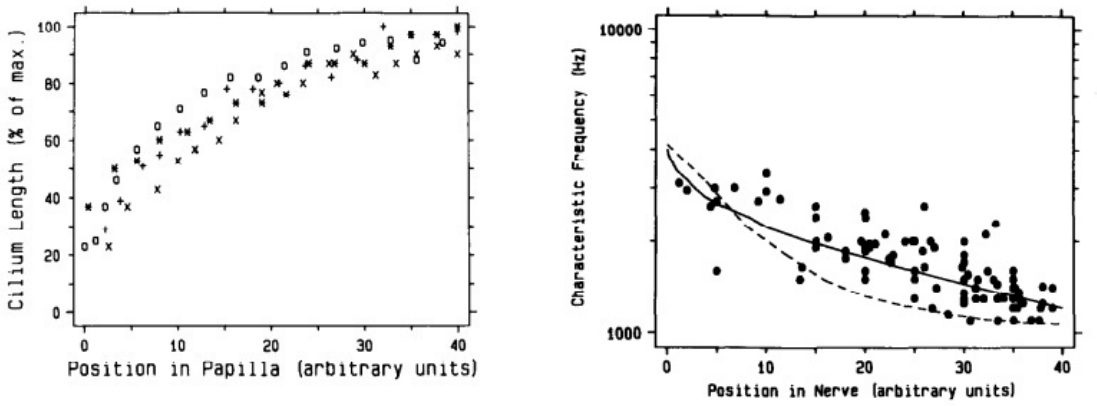

(a) (b)

Figure A.1: (a)Distribution of length of the longest stereocilium in an individual hair cell. (b) Comparison of derived and measured characteristic frequency distributions. [Adapted from Figure 4 and Figure 18, Turner, 1987

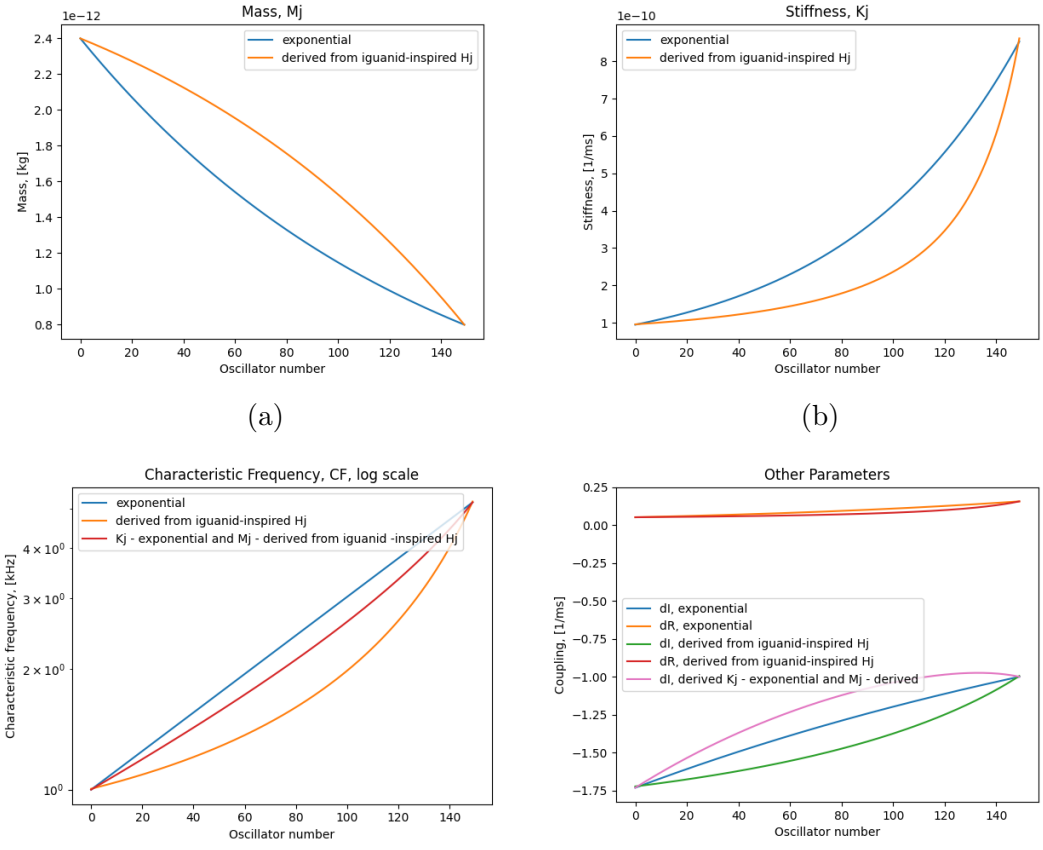

(a) (b)

(c) (d)

Figure A.2: Comparison of parameter distribution based on type of height distribution.

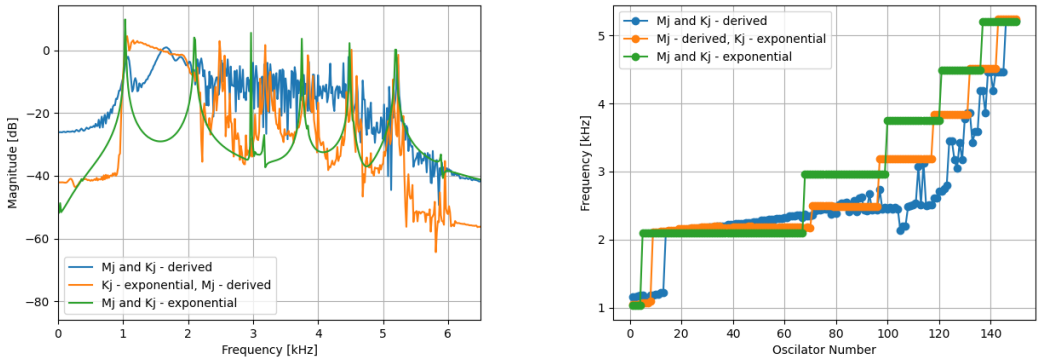

(a) (b)

Figure A.3: Comparison of (a) spectra and (b) clustering based on type of height distribution.

Due to the lack of information about hair cell bundle height and frequency distribution, we are using the assumption that $M_j \propto h_j$, $K_j \propto p_j/(h_j)^2$ and that height distribution is exponential, where p_j is a parameter that varies across chain to match exponential distributions of M_j, K_j, ω_j and h_j with their boundary values. The parameter p_j instead of being constant becomes an array value that helps to fix the issue with $\frac{K_{150}}{K_1} = 8.33$ and $\frac{h_1}{h_{150}} = 9$ and keeps set values for $h - 1$, h_{150} and ω_1 and ω_{150}.

A.1.2 Correlation Analysis

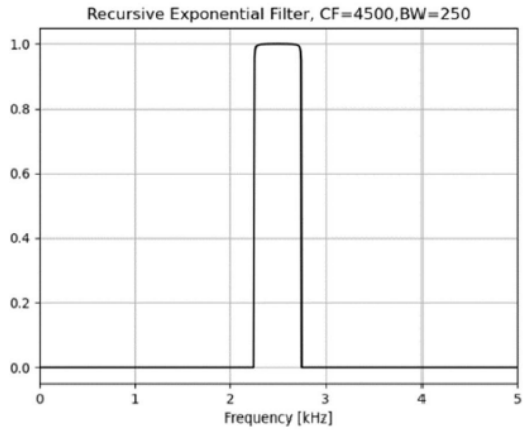

(a)

Figure A.4: Recursive exponential filter at the characteristic frequency of 4.5 kHz with a bandwidth of 250 Hz.

For this analysis, we used existing code in our group library and an already-established procedure. In this subsection, we will provide an overview of this procedure. We used averaged spectra to identify the characteristic frequency (CF) and bandwidth (BW) required to band-pass the desired peak. The filter was applied in the spectral domain by multiplying the long-waveform Fourier transform of the simulated waveform by the filter, as a filter we chose a recursive exponential filter. This filter was chosen because it is flat at the band frequencies like a box-car filter, however, it is not discontinuous at the corner frequencies (see Figure A.4). After that we used the inverse Fourier transform to obtain a waveform associated with a filtered peak. The Hilbert transform was used to compute the analytic signal of the filtered waveform. The complex nature of the analytic signal allows us to extract the instantaneous amplitude/envelope (ENV) and the instantaneous frequency (IF) of the filtered waveform (see Figure A.5). The instantaneous amplitude/envelope is the magnitude of the analytic signal and it is a trace that envelopes the filtered waveform thus describing how its amplitude changes with time.

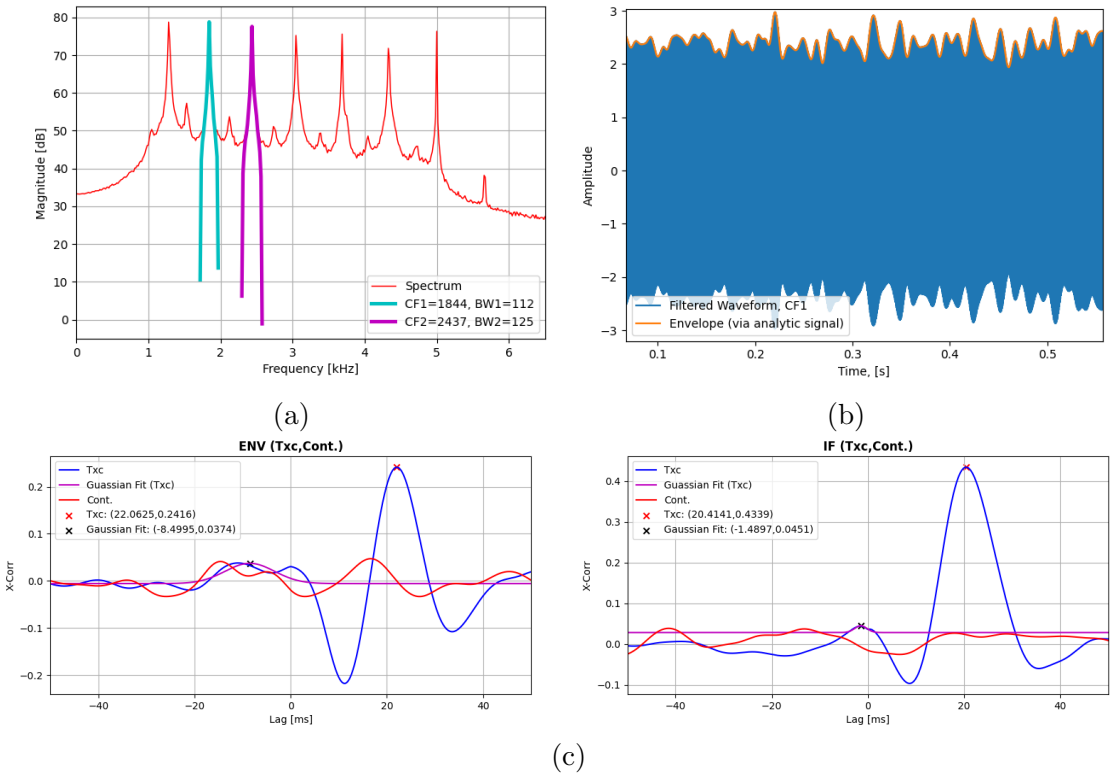

Figure A.5: Overview of the peak-filtering process and correlation analysis. (a) spectrum; (b) waveform and envelope; (c) AM and FM correlation.

In this work, there are 2 cross-correlation traces which are labelled as "Txc" and "Cont." (Figure A.5). The Txc stands for the averaged time domain crosscorrelation and

to produce it correlation is firstly computed between short segments of the envelopes and IFs and then an average is taken. The "Cont." trace, also referred to as the control, represents what a zero correlation ought to be like. This trace is computed by taking the averaged spectral-domain cross-correlation between shuffled envelope/IF segments. This trace also helps have a rough estimation of what the border value for maximum Txc should be to consider peaks correlated. In the case of this analysis, this value is 0.08.

A.2 Derivations

A.2.1 Vilfan and Duke (2008) model

$$M_j\ddot{x}_j = -K_j x_j - \Gamma_j \dot{x}_j + O(x^3) + F_j + \xi_j(t) \tag{A.1}$$

where for sallet: M_j – mass of j^{th} oscillator, K_j – spring constant, Γ_j – effective damping, $O(x^3)$ – cubic terms that describe the nonlinearity, F_j – force applied on a sallet by its neighbors, ξ_j – noise. Where F_j reads

$$F_j = k(x_{j+1} - x_j) + k(x_{j-1} - x_j) + \gamma(\dot{x}_{j+1} - \dot{x}_j) + \gamma(\dot{x}j - 1 - \dot{x}_j) \tag{A.2}$$

First, use complex value z_j to rewrite the first part of Eq (A.1)

$$z = x - \frac{1}{\omega} i\dot{x}, \tag{A.3}$$

taking into a count that $Rez = x_j$ and $Imz = -\frac{1}{\omega_j}\dot{x}_j$. For easier calculation let use $\dot{x}_j = y_j$, so

$$\begin{aligned} z_j &= x_j - \frac{1}{\omega_j} i y_j & \qquad x_j &= z_j + \frac{1}{\omega_j} i y_j \\ \dot{z}_j &= y_j - \frac{1}{\omega_j} i \dot{y}_j & \qquad \dot{y}_j &= \frac{\omega_j}{i}(y_j - \dot{z}_j) \end{aligned}$$

Now we have

$$\begin{aligned} M_j \frac{\omega_j}{i}(y_j - \dot{z}_j) = &- K_j z_j - \frac{i}{\omega_j} K_j y_j - \Gamma_j y_j + O(x^3) + \xi_j(t) + kRe(z_{j+} + z_{j-} - 2z_j) \\ &- \gamma(\omega_{j+1} Im(z_{j+1}) + \omega_{j-1} Im(z_{j-1}) - \omega_j Im(2z_j)) \end{aligned} \tag{A.4}$$

so

$$\begin{aligned} \dot{z}_j = &\frac{i}{\omega_j}\frac{K_j}{M_j} z_j - \frac{1}{\omega_j^2}\frac{K_j}{M_j} y_j + \frac{\Gamma_j}{M_j}\frac{i}{\omega_j} y_j - \frac{i\xi_j(t)}{\omega_j M_j} - \frac{k}{\omega_j M_j} iRe(z_{j+} + z_{j-} - 2z_j) \\ &+ i\frac{\gamma}{M_j} Im(\frac{\omega_{i+1}}{\omega_j} z_{j+1} + \frac{\omega_{i-1}}{\omega_j} z_{j-1} - 2z_j) + y_j + O(z^3) \end{aligned} \tag{A.5}$$

Now rewrite using

$$\omega_j = \sqrt{\frac{K_j}{M_j}} \tag{A.6}$$

$$\epsilon_j = -\frac{\Gamma_j}{2M_j} \tag{A.7}$$

$$d_{Ij} = -\frac{1}{2}\frac{k}{\sqrt{K_j M_j}} \tag{A.8}$$

$$d_{Rj} = \frac{1}{2}\frac{\gamma}{M_j} \tag{A.9}$$

$$\tilde{\xi_j}(t) = \frac{-i\xi_j(t)}{M_j\omega_j} \tag{A.10}$$

giving

$$\begin{aligned}\dot{z}_j =& i\omega_j z_j + 2\epsilon_j i Im z_j + 2id_{Ij} Re(z_{j+1} + z_{j-1} - 2z_j) \\ &+2id_{Rj} Im(\frac{\omega_{i+1}}{\omega_j} z_{j+1} + \frac{\omega_{i-1}}{\omega_j} z_{j-1} - 2z_j) + \tilde{\xi_j}(t) + O(z^3)\end{aligned} \tag{A.11}$$

Using complex conjugate $\bar{z}$:

$$Re z_j = \frac{z_j + \bar{z}_j}{2} \qquad Im z_j = \frac{z_j - \bar{z}_j}{2i}$$

$$x_j = \frac{z_j + \bar{z}_j}{2} \qquad y_j = -\frac{z_j - \bar{z}_j}{2\frac{i}{\omega}}$$

Now we have

$$\begin{aligned}\dot{z}_j =& i\omega_j z_j + \epsilon_j z_j + \epsilon_j \bar{z}_j + id_{Ij}(z_{j+1} + z_{j-1} - 2z_j) \\ &+id_{Ij}(\bar{z}_{j+1} + \bar{z}_{j-1} - 2\bar{z}_j) + d_{Rj}(\frac{\omega_{i+1}}{\omega_j} z_{j+1} + \frac{\omega_{i-1}}{\omega_j} z_{j-1} - 2z_j) \\ &+d_{Rj}(\frac{\omega_{i+1}}{\omega_j} \bar{z}_{j+1} + \frac{\omega_{i-1}}{\omega_j} \bar{z}_{j-1} - 2\bar{z}_j) + \tilde{\xi_j}(t) + O(z^3)\end{aligned} \tag{A.12}$$

Terms $z^3, z\bar{z}^2, \bar{z}^3$ can be neglected (Panfilov, 2001; McCann, 2013), which means that that the only term left is $z^2\bar{z} = |z|^2 z$.

$$\begin{aligned}\dot{z}_j =& i\omega_j z_j + \epsilon_j z_j + id_{Ij}(z_{j+1} + z_{j-1} - 2z_j) \\ &+d_{Rj}(\frac{\omega_{i+1}}{\omega_j} z_{j+1} + \frac{\omega_{i-1}}{\omega_j} z_{j-1} - 2z_j) + \tilde{\xi_j}(t) - B|z_j|^2 z_j\end{aligned} \tag{A.13}$$

But instead of equation A.13 we have

$$\begin{aligned}\dot{z}_j =& i\omega_j z_j + \epsilon_j z_j + id_I(z_{j+1} + z_{j-1} - 2z_j) \\ &+ d_R(z_{j+1} + z_{j-1} - z_j) + \tilde{\xi}_j(t) - B|z_j|^2 z_j\end{aligned} \tag{2.4}$$

A.2.1.1 An effect of $\frac{\omega_{i\pm1}}{\omega_j}$

Let us estimate the difference between ω_j and $\frac{\omega_{i\pm1}}{\omega_j}$ for a system of N oscillators. For our calculations, we are using $N = 150$ and $\frac{\omega_N}{\omega_1} = 5$.

$$\begin{aligned}\frac{\omega_{j+1}}{\omega_j} &= \frac{\omega_j + \delta\omega}{\omega_j} = \frac{\omega_j + \frac{4\omega_1}{149}}{\omega_j} \\ \frac{\omega_2}{\omega_1} &= \frac{\omega_1 + \delta\omega}{\omega_1} = \frac{\omega_1 + \frac{4\omega_1}{149}}{\omega_1} = \frac{153}{149} = 1.027 \\ \frac{\omega_{150}}{\omega_{149}} &= \frac{\omega_{150}}{\omega_{150} - \delta\omega} = \frac{5\omega_1}{5\omega_1 - \frac{4\omega_1}{159}} = \frac{745}{741} = 1.005 \\ \frac{\omega_1}{\omega_2} &= \frac{149}{153} = 0.973 \\ \frac{\omega_{149}}{\omega_{150}} &= \frac{741}{745} = 0.995 \\ 0.5\% \geq |\Delta| &\leq 2.7\% \text{ (for linear frequency distribution)} \\ \frac{\omega_{j+1}}{\omega_j} &= \frac{\omega_1(\frac{\omega_N}{\omega_1})^{\frac{j}{N-1}}}{\omega_1(\frac{\omega_N}{\omega_1})^{\frac{j-1}{N-1}}} = \left(\frac{\omega_N}{\omega_1}\right)^{\frac{1}{N-1}} = 5^{\frac{1}{149}} = 1.011 \\ \frac{\omega_{j+1}}{\omega_j} &= 5^{\frac{-1}{79}} = 0.989 \\ |\Delta| &\approx 1.1\% \text{ (for exponential frequency distribution)}\end{aligned}$$

Giving us $0.5\% \geq |\Delta| \leq 2.7\%$ for linear and $|\Delta| \approx 1.1\%$ for exponential frequency distribution. The other question is whether it's enough to make crucial changes, how much does this error contribute to the system's motion?

To understand whether these changes are crucial to our system, we are going to look at our results from a statistical point of view. Figure represents compared result

A.2.2 Global coupling via papilla

Global coupling via papilla is a modified version of Vilfan and Duke (2008) model. To define our system we are going to use the same logic as for local coupling. But in this case, the hair cell bundle is coupled to the papilla, not though additional visco-elastic element,

it is coupled via K_j and Γ_{jp}, making $F_{jp}h_j = -\tilde{K}_j(\theta_j - \theta_p) - \tilde{\Gamma}_{jp}(\dot{\theta}_j - \dot{\theta}_p)$. For this model we use small angle approximation such that $F_{jp} = -K_j(x_j - \frac{h_j}{r_j}y_p) - \Gamma_{jp}(\dot{x}_j - \frac{h_j}{r_j}\dot{x}_p)$.

$$\begin{aligned} M_j\ddot{x}_j &= -K_j(x_j - \frac{h_j}{r_j}y_p) - \Gamma_{jj}\dot{x}_j - \Gamma_{jp}(\dot{x}_j - \frac{h_j}{r_j}\dot{x}_p) + O(x^3) + F_j + \xi_j(t) \\ M_p\ddot{y}_p &= -K_p y_p - \Gamma_P \dot{y}_P + F_P + \xi_P(t) \end{aligned} \tag{A.14}$$

where for sallet: M_j – mass of j^{th} oscillator, K_j – spring constant/elastic coupling between bundle and papilla, $\Gamma_j = \Gamma jj + \Gamma jp$ – effective damping, Γ_{jj} – damping/viscouse coupling between bundle and papilla,Γ_{jj} – damping from amplifier, $O(x^3)$ – cubic terms that describe the nonlinearity, F_j – force applied on a sallet by its neighbors, ξ_j – noise; for papilla: M_p – mass oscillator, K_p – spring constant of papilla, Γ_p – damping of papilla, F_p – force exerted on a papilla by bundles, ξ_p – noise. F_j, F_p reads

$$F_j = k(x_{j+1} - x_j) + k(x_{j-1} - x_j) + \gamma(\dot{x}_{j+1} - \dot{x}_j) + \gamma(\dot{x}j - 1 - \dot{x}_j) \tag{A.15}$$

$$F_p = -\sum_j^N F_{jp} \tag{A.16}$$

Such that in the equation of motion for hair cell bundle we have two additional terms $+\frac{h_j}{r_j}(K_j x_p + \Gamma_{jp}\dot{x}_p)$ compared to the equation with only local coupling (Eq (A.1)). So using the same approaches as in the previous case we can rewrite our equation.

Note that variables x_j, x_p; y_j, y_p and z_j, z_p represent displacement, velocity and its complex value; and do NOT represent x and y axes in the cubic coordinate systems to describe directions of systems motion.

$$\begin{aligned} M_j\frac{\omega_j}{i}(y_j - \dot{z}_j) = &-K_j z_j - \frac{i}{\omega_j}K_j y_j - \Gamma_j y_j + \frac{h_j}{r_j}(K_j z_p + \frac{i}{w_p}K_j y_p + \Gamma_{jp}y_p) + O(x^3) + \xi_j(t) \\ &+ kRe(z_{j+} + z_{j-} - 2z_j) - \gamma(\omega_{j+1}Im(z_{j+1}) + \omega_{j-1}Im(z_{j-1}) - \omega_j Im(2z_j)) \end{aligned} \tag{A.17}$$

so

$$\begin{aligned} \dot{z}_j = &\frac{i}{\omega_j}\frac{K_j}{M_j}z_j - \frac{1}{\omega_j^2}\frac{K_j}{M_j}y_j + \frac{\Gamma_j}{M_j}\frac{i}{\omega_j}y_j + y_j + \frac{h_j}{r_j}(-\frac{iK_j}{\omega_j M_j}z_p + \frac{K_j}{\omega_p\omega_j M_j}y_p - \frac{i\Gamma_{jp}}{\omega_j M_j}y_p) \\ &-\frac{k}{\omega_j M_j}iRe(z_{j+} + z_{j-} - 2z_j) + i\frac{\gamma}{M_j}Im(\frac{\omega_{i+1}}{\omega_j}z_{j+1} + \frac{\omega_{i-1}}{\omega_j}z_{j-1} - 2z_j) - \frac{i\xi_j(t)}{\omega_j M_j} + O(z^3) \end{aligned} \tag{A.18}$$

Using equations (A.6-A.10) we have

$$\begin{aligned}\dot{z}_j =& i\omega_j z_j + 2\epsilon_j i Im z_j + \frac{h_j}{r_j}(-i\omega_j z_p - \omega_j Im z_p - 2\epsilon_{jp}\frac{\omega_p}{\omega_j} i Im z_p) + \tilde{\xi}_j(t) + O(z^3) \\ &+2id_{Ij}Re(z_{j+1} + z_{j-1} - 2z_j) + 2id_{Rj}Im(\frac{\omega_{i+1}}{\omega_j}z_{j+1} + \frac{\omega_{i-1}}{\omega_j}z_{j-1} - 2z_j)\end{aligned} \tag{A.19}$$

Now we rewrite using complex conjugate $\bar{z}$

$$\begin{aligned}\dot{z}_j =& i\omega_j z_j + \epsilon_j z_j + \epsilon_j \bar{z}_j + \frac{h_j}{r_j}(-i\omega_j z_p + \frac{i}{2}\omega_j z_p - \frac{i}{2}\omega_j \bar{z}_p - \epsilon_{jp}\frac{\omega_p}{\omega_j} z_p + \epsilon_{jp}\frac{\omega_p}{\omega_j}\bar{z}_p) \\ &+d_{Rj}(\frac{\omega_{i+1}}{\omega_j}z_{j+1} + \frac{\omega_{i-1}}{\omega_j}z_{j-1} - 2z_j) + d_{Rj}(\frac{\omega_{i+1}}{\omega_j}\bar{z}_{j+1} + \frac{\omega_{i-1}}{\omega_j}\bar{z}_{j-1} - 2\bar{z}_j) \\ &+id_{Ij}(z_{j+1} + z_{j-1} - 2z_j) + id_{Ij}(\bar{z}_{j+1} + \bar{z}_{j-1} - 2\bar{z}_j) + \tilde{\xi}_j(t) + O(z^3)\end{aligned} \tag{A.20}$$

Terms $z^3, z\bar{z}^2, \bar{z}^3$ can be neglected (Panfilov, 2001; McCann, 2013), which means that that the only term left is $z^2\bar{z} = |z|^2 z$.

$$\begin{aligned}\dot{z}_j =& i\omega_j(z_j - \frac{1}{2}\frac{h_j}{r_j}z_p) + \epsilon_j z_j - \epsilon_{jp}\frac{\omega_p}{\omega_j}\frac{h_j}{r_j}z_p + id_{Ij}(z_{j+1} + z_{j-1} - 2z_j) \\ &+d_{Rj}(\frac{\omega_{i+1}}{\omega_j}z_{j+1} + \frac{\omega_{i-1}}{\omega_j}z_{j-1} - 2z_j) + \tilde{\xi}_j(t) - B|z_j|^2 z_j\end{aligned} \tag{A.21}$$

But based on subsection A1.1 we can rewrite equation A.21

$$\begin{aligned}\dot{z}_j =& i\omega_j(z_j - \frac{1}{2}\frac{h_j}{r_j}z_p) + \epsilon_j z_j - \epsilon_{jp}\frac{\omega_p}{\omega_j}\frac{h_j}{r_j}z_p + id_I(z_{j+1} + z_{j-1} - 2z_j) \\ &+d_R(z_{j+1} + z_{j-1} - z_j) + \tilde{\xi}_j(t) - B|z_j|^2 z_j\end{aligned} \tag{2.6}$$

For pappila equation of motion would be:

$$\dot{z}_p = i\omega_p z_p + \epsilon_p z_p + \frac{M_j}{M_p}\sum[\frac{i}{2}\frac{{\omega_j}^2}{\omega_p}(z_j - z_p) - \epsilon_{jp}(\frac{\omega_j}{\omega_p}z_j - z_p)] \tag{2.7}$$

A.3 Amplitude death

SOAEs are a universal feature across the animal kingdom (despite highly variable inner ear morphology), but at the same time across the species is possible to see that some ears do not emit spontaneously. One of the possible explanation is that the system (coupled hair cell bundles) experience an amplitude death phenomenon.

Ahn (2013) introduces an amplitude death as the cessation of spontaneous oscillations by coupling. However, it is better to state that amplitude death is a state of oscillation suppression so that the system technically oscillates but the amplitude of those oscillations is so small that they can be neglected. In this section, I will look into changes in Amplitude for different sets of parameters for both systems of 2 coupled oscillators and systems of N (N=150) coupled oscillators.

A.3.1 Two coupled oscillators

Let us simplify the system to 2 coupled oscillators (equation A.22). This simplified scenario would be used to study (both analytically and numerically) the effect of different coupling on the collective dynamics of the system.

$$\begin{aligned} \dot{z}_1 &= i\omega_1 z_1 + \epsilon z_1 + id_I(z_2 - z_1) + d_R(z_2 - z_1) - B|z_1|^2 z_1 \\ \dot{z}_2 &= i\omega_1 z_2 + \epsilon z_2 + id_I(z_1 - z_2) + d_R(z_1 - z_2) - B|z_2|^2 z_2 \end{aligned} \tag{A.22}$$

The presence of coupling in between two oscillators can lead to 3 different scenarios: I) both oscillate at the same frequency (synchronization), II) the amplitude of both is dramatically suppressed so they are assumed to stop oscillating (amplitude death regime), III) both change the way of oscillation containing information about each other oscillation.

For a system with $d_I = 0$ and $d_R \neq 0$ (Aronson, 1989) can be analytically proved (see Appendix, Section A.2), that amplitude death could be achieved if $\epsilon < d_R < \frac{\epsilon}{2}(1 + (\frac{\Delta}{2\epsilon})^2)$ and $\epsilon < \frac{1}{2}\Delta$. Numerical results (Figure A.6) correspond to analytical results, leading to the same regions (I - $d_R \geq 1258$, II - $1200 < d_R < 1258$ and III - $dR \leq 1200$. At the same time system with only reactive coupling does not have an amplitude death regime (see further in this section), and numerical results lead to the same conclusion.

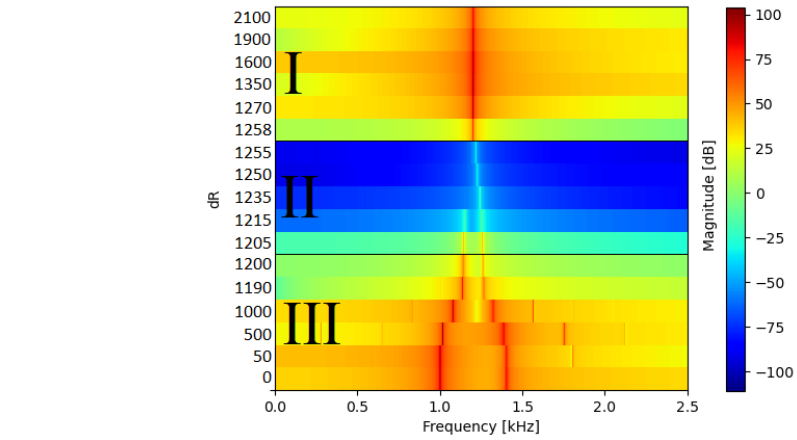

(a)

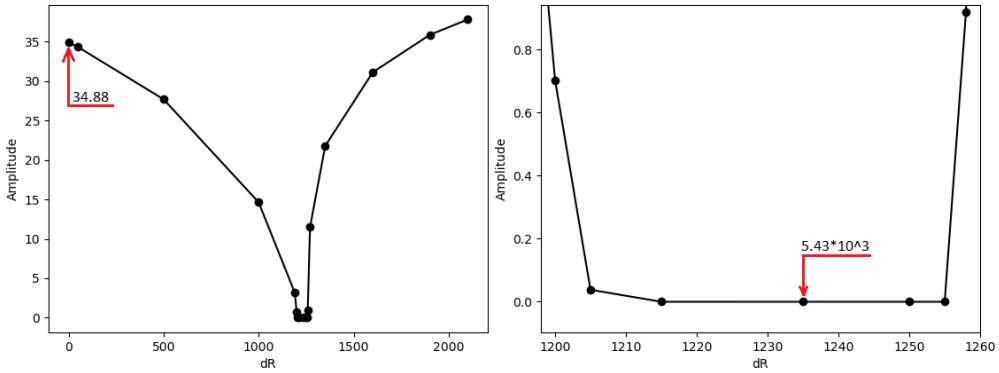

(b)

Figure A.6: Results for numerical simulation for system of two coupled oscillation, $B = 1$ $d_I = 0$, $w_1 = 1 * 2\pi * 10^3$, $w_1 = 1.4 * 2\pi * 10^3$, $\epsilon = 1200$. (a) Heatmap of spectra for each d_R, (b) dependence of oscillation amplitude on dissipative coupling d_R.

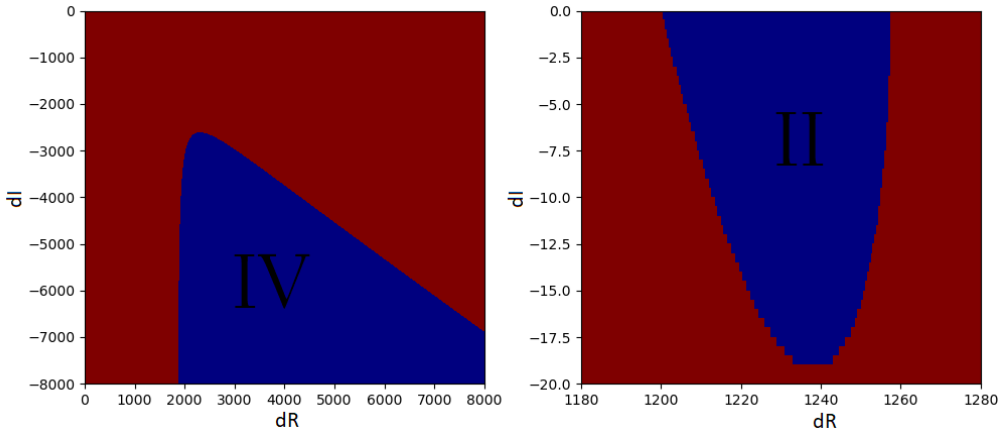

Figure A.7: Combinations of dissipative and reactive coupling that satisfy (blue) or not satisfy (red) criteria for amplitude death, with $w_1 = 2\pi * 10^3$, $w_1 = 1.4 * 2\pi * 10^3$, $\epsilon = 1200$.

For $d_R \neq 0$ and $d_I \neq 0$ the amplitude death could be achieved for system if parameters satisfy conditions in equation A.23, for example, using $w_1 = 1*2\pi*10^3$, $w_1 = 1.4*2\pi*10^3$, $\epsilon = 1200$ we could see what parameter combination leads to amplitude death (Figure A.7, blue region). In this case we see that 2 regions for amplitude death, let us call them I - amplitude death in a system with weak elastic coupling and IV amplitude death in a strongly coupled system.

$$d_R - \sqrt{{d_R}^2 - {d_I}^2 - \frac{1}{4}\Delta^2 + \sqrt{({d_R}^2 - {d_I}^2 - \frac{1}{4}\Delta^2)^2 + (\frac{1}{2}d_R d_I)^2}} > \epsilon \tag{A.23}$$

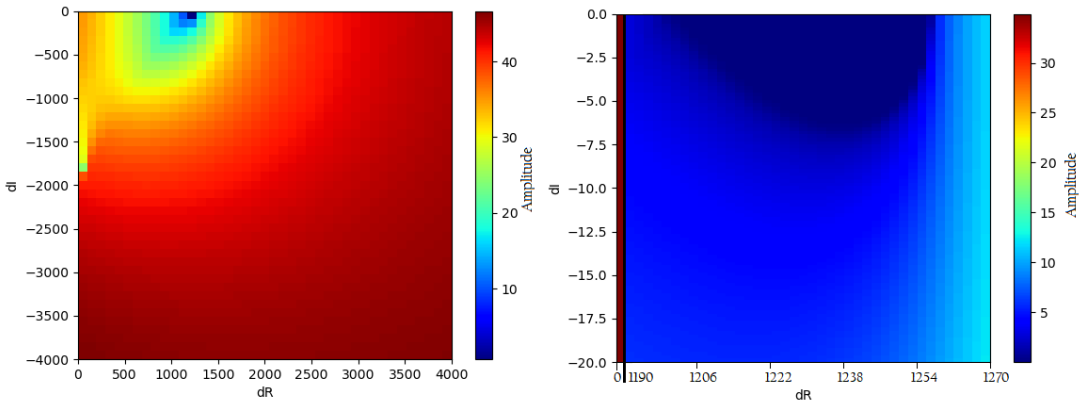

(a)

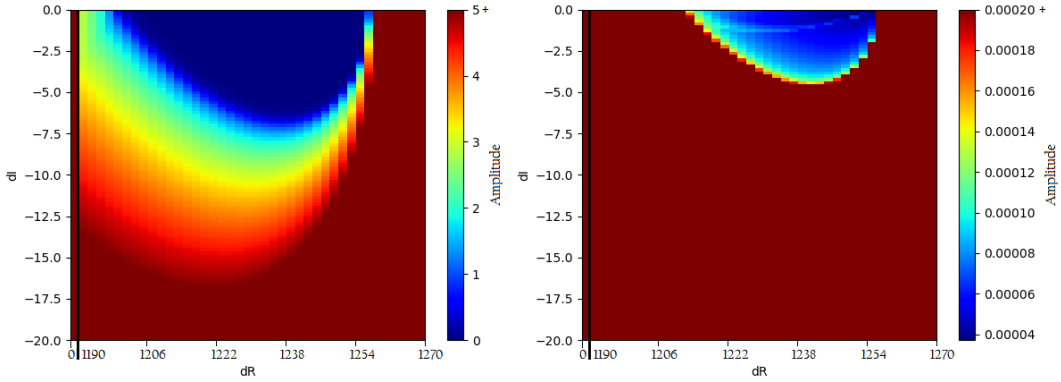

(b)

Figure A.8: (a) Amplitude of system (2 coupled oscillators) oscillations for different combinations of dissipative and reactive coupling, (b) rescaled color bar.

Figure A.8 shows the simulated amplitude of system oscillations for different coupling combinations. The left heatmap in subfigure (a) does not show us the predicted by analytical approach amplitude death in the strongly coupled system (region IV Figure A.7), at the same time it seems like there is amplitude death for weak elastic coupling

(region I Figure A.7). The right heatmap in subfigure (a) demonstrates amplitude for this region and subfigure (b) contains two heatmaps with rescaled color bars to better identify of regions of amplitude suppression. There is a mismatch in between numerical results and analytical predictions for coupling combinations that leads to amplitude death.

A.3.2 N coupled oscillators

A system of N coupled oscillators makes an analytical approach more complicated, and even for a system of two oscillators analytical approach does not match with numerical results, the parameters for this section have been chosen intuitively.

Figure A.9 amplitude for a system of 150 coupled oscillators for different coupling combinations for the case when $\epsilon = 0.01$. Here we see that stronger coupling leads to suppression of oscillations, which means amplitude death condition

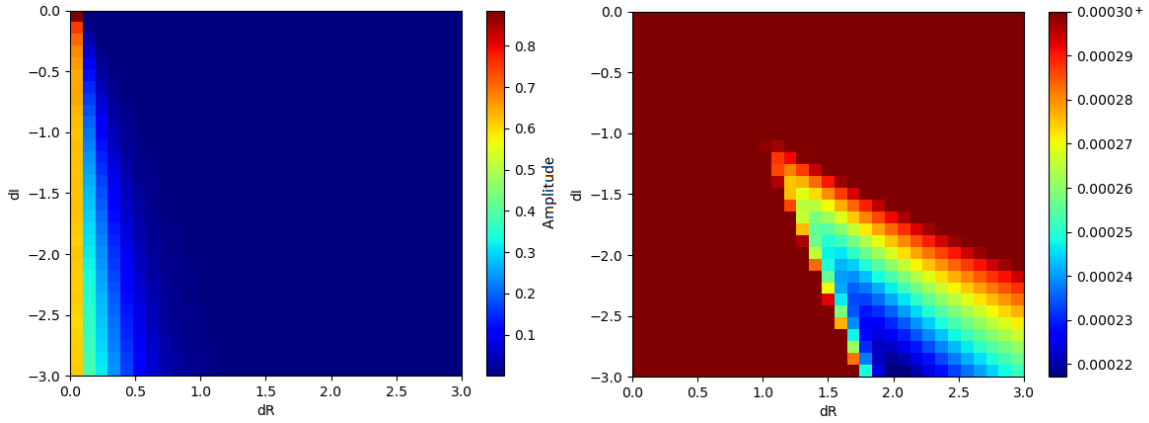

Figure A.9: The amplitude of system (150 coupled oscillators) oscillations for different combinations of dissipative and reactive coupling.

A.3.3 Analytical Solution for Two Coupled Oscillators

First, let's do an analytical calculation for the simplest system, the system of two coupled limit cycle oscillators, which can be described by the following equation:

$$\begin{aligned} \dot{z}_1 &= i\omega_1 z_1 + \epsilon z_1 + id_I(z_2 - z_1) + d_R(z_2 - z_1) - B|z_1|^2 z_1 \\ \dot{z}_2 &= i\omega_1 z_2 + \epsilon z_2 + id_I(z_1 - z_2) + d_R(z_1 - z_2) - B|z_2|^2 z_2 \end{aligned} \tag{A.22}$$

Lets calculate a Jacobian matrix at origin of right part

$$J = \begin{bmatrix} i\omega_1 + \epsilon - d_R - id_I & d_R + id_I \\ d_R + id_I & i\omega_2 + \epsilon - d_R - id_I \end{bmatrix} \tag{A.24}$$

To find its eigenvalue λ, let use the equation $det(J-\lambda I)=0$. For simplicity lets determine $a=(\epsilon-d_R)-\lambda$, so

$$a^2 - ai[(\omega_1 - d_I) + (\omega_2 - d_I)] - (\omega_1 - d_I) * (\omega_2 - d_I) - {d_R}^2 - 2id_R d_I + {d_I}^2 \tag{A.25}$$

giving

$$a = -\frac{i}{2}(\omega_1 + \omega_2 - 2d_I) \pm \sqrt{{d_R}^2 - {d_I}^2 - \frac{1}{4}(\omega_1 - \omega_2)^2 + \frac{i}{2}d_R d_I} \tag{A.26}$$

rewrite using $a=(\epsilon-d_R)-\lambda$ and defining $\Delta=|\omega_1-\omega_2|$

$$\lambda = \epsilon - d_R \pm \sqrt{{d_R}^2 - {d_I}^2 - \frac{1}{4}(\Delta)^2 + \frac{i}{2}d_R d_I} - \frac{i}{2}(\omega_1 + \omega_2 - 2d_I) \tag{A.27}$$

Another way (as you can see above this way leads to the same results) is to write in terms of $Rez_j = x_j$ and $Imz_j = q_j$

$$\begin{aligned}
\dot{x}_1 &= -\omega_1 q_1 + \epsilon x_1 - d_I(q_2 - q_1) + d_R(x_2 - x_1) - B({x_1}^2 + {q_1}^2)x_1 \\
\dot{q}_1 &= \omega_1 x_1 + \epsilon q_1 + d_I(x_2 - x_1) + d_R(q_2 - q_1) - B({x_1}^2 + {q_1}^2)q_1 \\
\dot{x}_2 &= -\omega_2 q_2 + \epsilon x_2 - d_I(q_1 - q_2) + d_R(x_1 - x_2) - B({x_2}^2 + {q_2}^2)x_2 \\
\dot{q}_2 &= \omega_2 x_2 + \epsilon q_2 + d_I(x_1 - x_2) + d_R(q_1 - q_2) - B({x_2}^2 + {q_2}^2)q_2
\end{aligned} \tag{A.28}$$

Jacobian matrix at the origin of the right part would be

$$J = \begin{bmatrix} \epsilon - d_R & -(\omega_1 - d_I) & d_R & -d_I \\ \omega_1 - d_I & \epsilon - d_R & d_I & d_R \\ d_R & -d_I & \epsilon - d_R & -(\omega_2 - d_I) \\ d_I & d_R & \omega_2 - d_I & \epsilon - d_R \end{bmatrix} \tag{A.29}$$

To find its eigenvalue λ, let use the equation $det(J-\lambda I)=0$. For simplicity lets determine $a=(\epsilon-d_R)-\lambda$, so

$$\begin{aligned}
&a^4 - 2{d_R}^2 a^2 + 2{d_I}^2 a^2 + [(\omega_1 - d_I)^2 + (\omega_2 - d_I)^2]a^2 - 4d_R d_I(\omega_1 + \omega_2 + 2d_I)a \\
&\quad + 2{d_R}^2{d_I}^2 + 2{d_R}^2(\omega_1 - d_I)(\omega_2 - d_I) - 2{d_I}^2(\omega_1 - d_I)(\omega_2 - d_I) \\
&\quad + (\omega_1 - d_I)^2(\omega_2 - d_I)^2 + {d_R}^4 + {d_I}^4 = 0
\end{aligned} \tag{A.30}$$

For amplitude death to occur, the synchronized state should be a fixed stable point. For this, the eigenvalues of the Jacobian (equation A.29) should be negative.

For simpler case, let assume that $d_I = 0$ and $d_R \neq 0$ (Aronson, 1989), so

$$a^4 - 2{d_R}^2 a^2 + ({\omega_1}^2 + {\omega_2}^2)a^2 + 2{d_R}^2(\omega_1 * \omega_2) + (\omega_1)^2(\omega_2)^2 + {d_R}^4 = 0 \tag{A.31}$$

$$[a^4 - 2{d_R}^2 a^2 - 2\omega_1\omega_2 a^2 + {d_R}^4 + 2\omega_1\omega_2{d_R}^2 + {\omega_1}^2{\omega_2}^2] + {\omega_1}^2 a^2 + {\omega_2}^2 a^2 + 2\omega_1\omega_2 a^2 = 0 \tag{A.32}$$

Leading us to equation

$$[a^2 - ({d_R}^2 + \omega_1\omega_2)]^2 = -(\omega_1 + \omega_2)^2 a^2 \tag{A.33}$$

---

with

$$a = \pm\sqrt{{d_R}^2 - \frac{1}{4}(\omega_1 - {\omega_2}^2)} \pm \frac{i}{2}(\omega_1 + \omega_2) \tag{A.34}$$

rewrite using $a = (\epsilon - d_R) - \lambda$ and defining $\Delta = |\omega_1 - \omega_2|$

$$\lambda = \epsilon - d_R \pm \sqrt{{d_R}^2 - \frac{1}{4}(\Delta^2)} \pm \frac{i}{2}(\omega_1 + \omega_2) \tag{A.35}$$

Another scenario is when $d_R = 0$ and $d_I \neq 0$

$$\begin{aligned} &a^4 + 2{d_I}^2 a^2 + [(\omega_1 - d_I)^2 + (\omega_2 - d_I)^2]a^2 + {d_I}^4 \\ &-2{d_I}^2((\omega_1 - d_I) * (\omega_2 - d_I)) + (\omega_1 - d_I)^2(\omega_2 - d_I)^2 = 0 \end{aligned} \tag{A.36}$$

Leading us to equation

$$[a^2 + ({d_I}^2 - (\omega_1 - d_I)(\omega_2 - d_I))]^2 = -[(\omega_1 - d_I) + (\omega_2 - d_I)]^2 a^2 \tag{A.37}$$

with

$$a = \pm\sqrt{-{d_I}^2 - \frac{1}{4}(\omega_1 - \omega_2)^2} \pm \frac{i}{2}(\omega_1 + \omega_2 - 2d_I) \tag{A.38}$$

rewrite using $a = \epsilon - \lambda$ and defining $\Delta = |\omega_1 - \omega_2|$

$$\lambda = \epsilon \pm \sqrt{-{d_I}^2 - \frac{1}{4}(\Delta^2)} \pm \frac{i}{2}(\omega_1 + \omega_2 - 2d_I) \tag{A.39}$$

Now we come back to $d_R \neq 0$, $d_I \neq 0$ scenario, as we did previously, lets rearrange and rewrite equation A.30

$$[a^2 - ({d_R}^2 + (\omega_1 - d_I)(\omega_2 - d_I) - {d_I}^2)]^2 = -([(\omega_1 - d_I) + (\omega_2 - d_I)]a - 2d_R d_I)^2 \tag{A.40}$$

with

$$a = \pm\sqrt{{d_R}^2 - {d_I}^2 - \frac{1}{4}(\omega_1 - \omega_2)^2 \pm \frac{i}{2}|d_R d_I|} \pm \frac{i}{2}(\omega_1 + \omega_2 - 2d_I) \tag{A.41}$$

rewrite using $a = (\epsilon - d_R) - \lambda$ and defining $\Delta = |\omega_1 - \omega_2|$

$$\lambda = \epsilon - d_R \pm \sqrt{{d_R}^2 - {d_I}^2 - \frac{1}{4}(\Delta)^2 \pm \frac{i}{2}|d_R d_I|} \pm \frac{i}{2}(\omega_1 + \omega_2 - 2d_I) \tag{A.42}$$

Now let's analyze real part of value λ.

For $d_I = 0 = 0$ and $d_R \neq 0$:

In this case we would have two different scenarios:

$$\begin{aligned}
&(|\Delta| \geq 2d_R) \quad Re\lambda = \epsilon - d_R \\
&(|\Delta| < 2d_R) \quad Re\lambda_1 = \epsilon - d_R + \sqrt{{d_R}^2 - \frac{1}{4}(\Delta)^2} \\
&(|\Delta| < 2d_R) \quad Re\lambda_2 = \epsilon - d_R - \sqrt{{d_R}^2 - \frac{1}{4}(\Delta)^2}
\end{aligned} \tag{A.43}$$

From $Re\lambda$ we know that $d_R > \epsilon$, $\epsilon - d_R$ is negative which makes $Re\lambda_2$ negative and $Re\lambda_1$ would be negative if

$$\begin{aligned}
\sqrt{{d_R}^2 - \frac{1}{4}(\Delta^2)} &< d_R - \epsilon \\
{d_R}^2 - \frac{1}{4}(\Delta^2) &< (d_R - \epsilon)^2 \\
d_R &< \frac{\epsilon}{2}(1 + (\frac{\Delta}{2\epsilon})^2)
\end{aligned} \tag{A.44}$$

We only can get all negative eigenvalues (equation A.43) $\epsilon < d_R < \frac{\epsilon}{2}(1 + (\frac{\Delta}{2\epsilon})^2)$ only if $2\epsilon < \Delta$.

For $d_R = 0$ and $d_I \neq 0$:
In this case we would have two different scenarios:

$$\begin{aligned}
&(d_I \geq -|\Delta|) \quad Re\lambda = \epsilon \\
&(d_I < -|\Delta|) \quad Re\lambda_1 = \epsilon + \sqrt{-{d_I}^2 - \frac{1}{4}(\Delta)^2} \\
&(d_I < -|\Delta|) \quad Re\lambda_2 = \epsilon - \sqrt{-{d_I}^2 - \frac{1}{4}(\Delta)^2}
\end{aligned} \tag{A.45}$$

For analysis, we need the real part of all eigenvalues (equation A.45) to be negative. We know that $\epsilon > 0$ which means that such a system is not able to achieve amplitude death conditions.

For $d_R \neq 0$ and $d_I \neq 0$:
This is not an obvious task because we have the square root of the complex number.

$$\lambda = \epsilon - d_R \pm \sqrt{{d_R}^2 - {d_I}^2 - \frac{1}{4}(\Delta)^2 + \frac{i}{2}d_R d_I} - \frac{i}{2}(\omega_1 + \omega_2 - 2d_I) \tag{A.46}$$

and as we know $\sqrt{x+iy} = m + in$, so we need to satisfy $\epsilon - d_R \pm m < 0$, with We are interested in a scenario when

$$d_R - \sqrt{{d_R}^2 - {d_I}^2 - \frac{1}{4}\Delta^2 + \sqrt{({d_R}^2 - {d_I}^2 - \frac{1}{4}\Delta^2)^2 + (\frac{1}{2}d_R d_I)^2}} > \epsilon \tag{A.23}$$